JCB Journal of Cell Biology

ARTICLE

RAB-10 cooperates with EHBP-1 to capture vesicular carriers during post-Golgi exocytic trafficking

Shuai Liu[1*], Jie Wei[1*], Liangyujie Zhong[1], Sirao Hai[1], Shibo Song[1], Chaoyi Xie[1], Zeyu Huang[1], Zihang Cheng[1], Jing Zhang[1], Anna Du[2], Pei Zhang[2], Yanling Yan[1], and Anbing Shi[1,3,4]

Post-Golgi exocytic trafficking, fundamental for secretion and cell surface component integration, remains incompletely understood at the molecular level. Here, we investigated this process using *Caenorhabditis elegans* and mammalian cell models, revealing a novel exocytic carrier capturing mechanism involving the small GTPase RAB-10/Rab10 and its effector EHBP-1/EHBP1. EHBP-1, localized in recycling endosomes, selectively captures RAB-10-positive lipoprotein exocytic carriers through its interaction with active RAB-10, thereby promoting the delivery of exocytic cargo to recycling endosomes. A detailed mechanistic examination demonstrated the synergy between EHBP-1's RAB-10-binding coiled-coil domain and its PI(4,5)P2-binding C2 domain in the capturing process. Of note, we identified LST-6/DENND5 as a specialized guanine nucleotide exchange factor (GEF) for RAB-10 in this particular pathway, distinct from the GEF involved in basolateral recycling. Following the RAB-10-EHBP-1-mediated capture, the exocyst complex carries out its function. Taken together, this study suggests a potential tethering mechanism for basolateral post-Golgi exocytic carriers, highlighting the coordination among membrane compartments in regulating this trafficking route.

Introduction

Studies on post-Golgi exocytic trafficking have highlighted the role of specific Rab GTPases, underscoring the importance of the crosstalk between the exocytic and endocytic systems (Huber et al., 1993; Ang et al., 2003; Wells et al., 2023). In MDCK cells, Rab8 localizes to the Golgi apparatus and recycling endosome and works with AP-1B to regulate the basolateral exocytosis of newly synthesized membrane proteins (Huber et al., 1993; Ang et al., 2003). Investigations conducted in HeLa cells demonstrated the involvement of Rab8 in associating, docking, and fusing exocytotic vesicles, a process dependent on Rab6 (Grigoriev et al., 2011). Further structural studies indicated that the interaction between Rab8 and EHBP1 results in the release of the CH domain of EHBP1, which aids in its attachment to actin filaments and promotes membrane tubulation (Rai et al., 2020). Studies on Rab11 and Rab13 provided additional evidence supporting the role of the recycling endosome as an intermediary in post-Golgi exocytic trafficking (Ang et al., 2004). In BHK cells, the absence of Rab11 led to the accumulation of VSVG in the Golgi (Chen et al., 1998). Likewise, in HBE cells, overexpression of a mutant Rab13 hindered the exocytic transport of VSVG via recycling endosomes (Nokes et al., 2008). A recent inquiry revealed defects in hepatic VLDL secretion following the expression of dominant negative Rab8b, Rab11, and Rab13 (Takacs et al., 2017). Besides the studies on Rabs, there is additional evidence supporting the participation of recycling endosomes in post-Golgi exocytic trafficking. For instance, the exocytic processes of TNFα, IL-6, and E-cadherin have been linked to recycling endosomes (Lock and Stow, 2005; Manderson et al., 2007; Murray et al., 2005). However, the precise mechanism responsible for directing exocytic cargo from the trans-Golgi network (TGN) to the recycling endosome is not fully understood. In particular, an expanding array of recycling regulators is being unveiled, yet their roles in post-Golgi exocytic trafficking remain unclear.

The precise localization of vesicular carriers to their designated target compartments to facilitate cargo release is essential for membrane transport. This process is orchestrated through a sophisticated interplay between tethers and SNAREs (Spang, 2002, 2008; Bonifacino and Glick, 2004; Yu and Hughson, 2010). Tethers, primarily located on the target membrane, actively seek proper vesicles and establish connections with them (Yu and Hughson, 2010). Tethers are categorized into coiled-coil (CC) tethers and multisubunit tethering complexes (MTCs) (Brunet and Sacher, 2014). EEA1, a prominent CC tether, is recruited to early endosomes that harbor PI3P. Then, the interaction between

[1]Department of Biochemistry and Molecular Biology, School of Basic Medicine, Tongji Medical College and State Key Laboratory for Diagnosis and Treatment of Severe Zoonotic Infectious Disease, Huazhong University of Science and Technology, Wuhan, China; [2]Wuhan Institute of Virology, Chinese Academy of Sciences, Wuhan, China; [3]Cell Architecture Research Center, Huazhong University of Science and Technology, Wuhan, China; [4]Key Laboratory of Education Ministry of China for Neurological Disorders, Tongji Medical College, Huazhong University of Science and Technology, Wuhan, China.

*S. Liu and J. Wei contributed equally to this paper. Correspondence to Anbing Shi: ashi@hust.edu.cn; Yanling Yan: yanyl@hust.edu.cn.

EEA1 and Rab5 facilitates the movement of Rab5-labeled vesicles toward early endosomes (Murray et al., 2016). Compared with CC tethers, MTCs have limitations regarding membrane bridging distances and are involved in more intricate functions during membrane fusion (Shvarev et al., 2022). MTCs fall into two functional groups, the first being the CATCHR complexes, such as the exocyst, which predominantly function in the secretory pathway (Spang, 2012, 2016; Szentgyörgyi and Spang, 2023). The second group includes MTCs that operate within the endomembrane system, such as the HOPS, CORVET, CHEVI, and FERARI complexes (Nickerson et al., 2009; Lürick et al., 2018; Szentgyorgyi and Spang, 2023). FERARI has been suggested to act on RAB-10/Rab10-positive endosomes in *Caenorhabditis elegans* and mammalian cells, facilitating endocytic recycling (Solinger et al., 2020, 2022). Recently, reconstituted tethering assays also suggested that Rabs inherently possess the capability to capture endosomes through the formation of trans-Rab-Rab self-assemblies (Mima, 2021).

Rab10 is closely related to Rab8 and Rab13 (Babbey et al., 2006). In both MDCK cells and *C. elegans*, RAB-10/Rab10 exhibits a specific association with early/sorting endosomes, promoting basolateral recycling (Babbey et al., 2006; Chen et al., 2006). The activation of RAB-10/Rab10 involves DENN-4/DENND4 serving as the guanine nucleotide exchange factor (GEF) (Sano et al., 2011; Yoshimura et al., 2010; Liu et al., 2018). Of note, a study in MDCK cells revealed Rab10's localization in the Golgi during polarization initiation, indicating its role in regulating basolateral exocytosis (Schuck et al., 2007). Additionally, analysis in *C. elegans* implicated RAB-10 in transport from secretory compartments, a process essential for dendritic growth (Zou et al., 2015). In this study, we demonstrated that EHBP-1, located in recycling endosomes, promotes the sequestration of lipoprotein exocytic carriers associated with RAB-10. LST-6/DENND5 serves as a GEF that specifically enhances RAB-10 activity during basolateral exocytosis, distinguishing it from DENN-4, which facilitates basolateral recycling. Intriguingly, these results suggest that EHBP-1 may serve as a tether, bringing RAB-10-positive exocytic carriers in close proximity to recycling endosomes.

Results

RAB-10 is required for basolateral lipoprotein exocytosis in intestinal epithelia

The regulation of exocytosis involves multiple Rab GTPases, including Rab1, Rab2, Rab6, Rab8, Rab11, Rab12, Rab13, Rab26, Rab27, and Rab37 (Hutagalung and Novick, 2011), with Rab8, Rab11, and Rab13 having specific roles in governing post-Golgi exocytic trafficking (Huber et al., 1993; Chen et al., 1998; Nokes et al., 2008; Grigoriev et al., 2011). In *C. elegans*, no homologs of Rab13 have been identified (Watterson et al., 2022; Gallegos et al., 2012). RAB-8 and RAB-11 were reported to facilitate apical secretion in the intestine (Wang et al., 2022; Li et al., 2024). Of note, RAB-10's role in basolateral exocytosis has been suggested through screening for yolk secretion defects (Balklava et al., 2007); nevertheless, the results exhibited inconsistencies across replicates. This lack of clarity regarding Rabs' involvement in basolateral exocytosis led us to examine the role of 22 identified Rabs in this process (Fig. S1 and Fig. S2 A).

In *C. elegans*, yolk synthesis occurs in the intestinal cells (Kimble and Sharrock, 1983), followed by its basolateral exocytosis into the pseudocoelom and uptake by the oocyte (Fig. 1 A) (Hall et al., 1999). The *vit-2* gene encodes vitellogenin YP170B, the major yolk protein (Goszczynski et al., 2016). Endogenous VIT-2 (VIT-2-mNeonGreen-3xFlag) is primarily located in basolateral punctate structures (top focal plane) of intestinal cells, which are likely indicative of yolk secretion vesicles (Fig. S1). Also, VIT-2 is present in small amounts in the body cavity, while being abundant in yolk granules within oocytes and early embryos. In *rab-10(RNAi)* animals, a decrease in VIT-2-labeled structures near the basolateral membrane and an accumulation of VIT-2 deep in the cytosol (middle focal plane) was noted, accompanied by a distinct reduction in VIT-2 in the body cavity, oocytes, and early embryos (Fig. S1 and Fig. S2 A). In contrast, the loss of RAB-8 did not yield an intestinal VIT-2 accumulation phenotype (Fig. S1 and Fig. S2 A). Notably, the absence of RAB-5 led to VIT-2 accumulation in the body cavity and decreased VIT-2 levels in oocytes (Fig. S1 and Fig. S2 A), indicating impaired endocytic uptake in oocytes. Moreover, *rab-1(RNAi)* animals exhibited an accumulation of VIT-2 within densely clustered vesicles in the intestine (Fig. S1 and Fig. S2 A). This finding aligns with the role of RAB-1/Rab1 in facilitating the tethering of ER-derived vesicles to the Golgi (Moyer et al., 2001). RAB-11.1 and RAB-11.2 show similarity to mammalian Rab11a (Satoh et al., 2005), and RAB-11.1 has been demonstrated to regulate apical exocytosis from recycling endosomes or TGN (Grant and Donaldson, 2009; Los et al., 2011; Szumowski et al., 2014). In RAB-11.1-deficient cells, a distinct phenotype was identified, showing the lack of intestinal VIT-2 signals and a mild reduction in yolk granules in oocytes and embryos (Fig. S1 and Fig. S2 A), suggesting a link between the absence of RAB-11.1 and yolk degradation in intestinal cells.

We then verified the role of RAB-10 in VIT-2 secretion using the putative null allele *ok1494* of *rab-10* (Fig. 1, B and B′), characterized by a 663-bp deletion in the coding region leading to a complete loss of function (Taylor et al., 2015). We observed a cytosolic accumulation of VIT-2-positive structures alongside a decrease in VIT-2 labeling in the body cavity and oocytes (Fig. 1, B and B′). A missense mutation in the GTP-binding domain of RAB-10 results in the weak allele *rab-10(q373)* (Chen et al., 2006). Likewise, in *rab-10(q373)* mutants, comparable, albeit subtle, changes in VIT-2 distribution across tissues were noted (Fig. 1, B and B′).

In MDCK cells, Rab10 exhibits a specific association with sorting endosomes, facilitating basolateral recycling (Babbey et al., 2006). To evaluate the evolutionary conservation of Rab10 in regulating exocytosis, we employed HepG2 cells to assay the efficiency of apoB-labeled lipoprotein secretion. Upon shRNA-mediated knockdown of Rab10, a significant decrease in apoB level was detected in the cell culture medium (Fig. 1, C and C′). Of note, the levels of apoB also decreased in Rab10 knockdown cells (Fig. 1. C and C′), while apoB mRNA abundance remained unchanged (Fig. S2 C), suggesting that the lack of Rab10 hinders the exocytic transport of lipoproteins, potentially leading to their degradation.

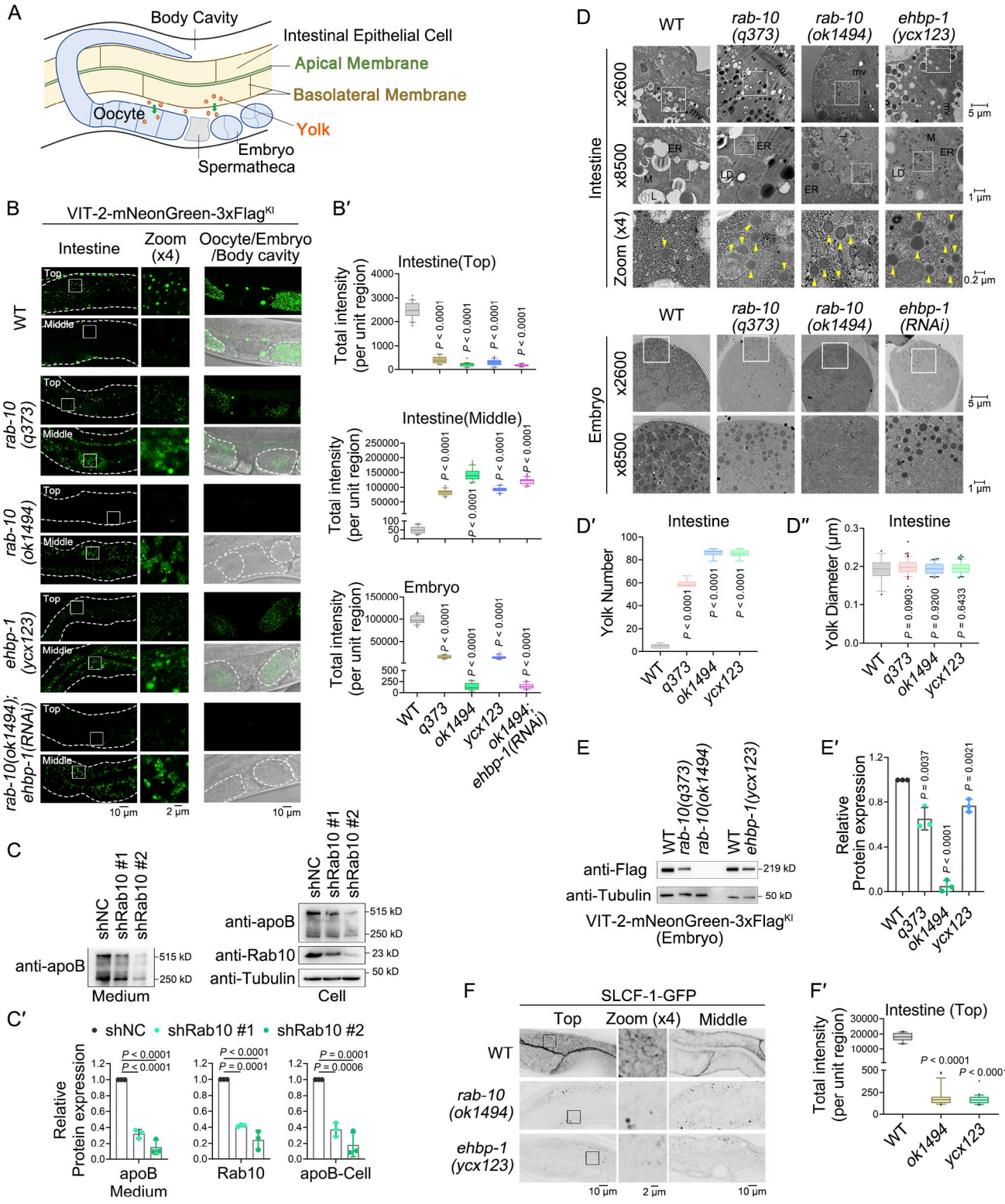

Figure 1. **RAB-10 and EHBP-1 participate in basolateral exocytosis in *C. elegans* intestinal epithelia. (A)** A diagram of *C. elegans* intestine, showing the secretion pathway of yolk. **(B and B′)** Confocal images showing the distribution of VIT-2-mNeonGreen-3xFlag^{KI} in the *C. elegans* intestine, oocytes, and embryos. "Top" shows the basal membrane, while "Middle" shows the apical membrane, cytosol, and lumen of the intestinal cells. White dashed lines indicate the outlines of the intestine, oocytes, or embryos. Data are shown as box-and-whisker plots with 10th–90th percentile (n = 24 cells from eight animals of each genotype; dots, outliers; boundaries, quartiles; one-way ANOVA test with Dunn's multiple comparison). **(C and C′)** Western blot analysis of apoB protein levels in HepG2 cells. Band intensity was measured using the "Plot Lanes" function in ImageJ from three independent experiments. Error bars represent 95% CIs (one-way ANOVA test with Dunn's multiple comparison). **(D–D″)** Transmission electron microscope (TEM) images of intestines and one-cell or two-cell embryos. The yellow arrowhead indicates a yolk granule (mv: microvilli; L: lysosome; M: mitochondria; ER: endoplasmic reticulum; LD: lipid droplet). Quantification of

yolk number and diameter in *C. elegans* intestine, data are shown as box-and-whisker plots with 10th–90th percentile (n = 6 animals; dots, outliers; boundaries, quartiles; one-way ANOVA test with Dunn's multiple comparison). **(E and E′)** Western blot analysis of VIT-2 protein levels in *C. elegans* early embryos using an anti-Flag antibody. The band intensity was measured using the "Plot Lanes" function in ImageJ from three independent experiments. The error bars represent 95% CIs (one-way ANOVA test with Dunn's multiple comparison). **(F and F′)** Confocal images showing the subcellular localization of SLCF-1-GFP. Statistical analysis was conducted as in B. Source data are available for this figure: SourceData F1.

EHBP-1, the RAB-10 effector, is essential for basolateral exocytosis

RAB-10 engages various effector proteins to regulate intracellular transport (Shi et al., 2010, 2012; Liu and Grant, 2015; Liu et al., 2013). To this end, we set out to test the involvement of documented RAB-10 effectors in basolateral exocytosis, including EHBP-1, TBC-2, CNT-1, and HUM-2, known for their roles in recycling within the worm intestine, as well as JIP-1, KLC-1, KLC-2, and KLP-4, implicated in axonal development (Chen et al., 2012; Liu and Grant, 2015; Deng et al., 2014; Shi et al., 2012). Notably, only the loss of EHBP-1 led to an intestinal buildup of VIT-2-labeled structures (Fig. S3, A and A′). We validated this result using a heat shock–inducible CRISPR-Cas9 *ehbp-1(ycx123)* conditional mutant (Li et al., 2015), denoted as *ycx123* (Fig. S2, D–E′). In the *ehbp-1* mutant, a reduction in basolateral VIT-2 puncta and an intracellular accumulation of VIT-2 was observed, along with a notable decrease in oocytes and embryos (Fig. 1, B and B′). A similar phenotype was noted with the transgenic strain *pwIs23* [vit-2::GFP] (Fig. S2, B and B′). Together, these results reveal the implication of EHBP-1 in basolateral exocytosis. Also, our findings imply that the mechanism governing exocytosis, facilitated by RAB-10 and EHBP-1, might diverge to some extent from the RAB-10-mediated recycling regulation.

To further define the deficiency phenotypes of RAB-10 and EHBP-1, we used transmission electron microscopy (TEM) to inspect cross-sections of *C. elegans*. Electron-dense yolk-filled vesicles (Hall et al., 1999), measuring around 200 nm in diameter, were observed in small numbers in the intestine (Fig. 1, D–D″). Although the morphology of yolk vesicles in *rab-10* and *ehbp-1* mutants remained largely unchanged, there was a noticeable increase in their abundance (Fig. 1, D–D″). Moreover, TEM images of the embryos displayed a decrease in yolk granules in RAB-10- and EHBP-1-deficient animals (Fig. 1 D). Consistently, *rab-10(ok1494)* mutants showed a substantial depletion in the embryonic VIT-2, with *rab-10(q373)* and *ehbp-1(ycx123)* animals also displaying a modest decline in this protein (Fig. 1, E and E′). Older adults allocate more yolk to embryos, resulting in faster offspring development. Besides, after experiencing starvation during early development, a larger proportion of offspring from older adults exhibited successful development into adults after the transition to normal feeding conditions (Perez et al., 2017). In agreement with the reduction in yolk content in embryos, the progeny of adults (24 h post-L4) with RAB-10 or EHBP-1 deficiency displayed a decrease in body length after 42 h of development (Fig. S2, F and F′). These descendants showed a reduced likelihood of undergoing normal development following starvation at the L1 stage (Fig. S2 G). Altogether, these results provide support for the involvement of RAB-10 and EHBP-1 in basolateral exocytosis of soluble yolk in intestinal cells.

We also investigated the implication of RAB-10 and EHBP-1 in the exocytic delivery of membrane proteins by studying the distribution of SLCF-1, a monocarboxylate transporter (Wang et al., 2021). SLCF-1 is mainly localized in basolateral punctate and meshwork-like structures. In *rab-10* and *ehbp-1* mutants, the SLCF-1-labeled structures were diminished (Fig. 1, F and F′), without affecting SLCF-1 mRNA levels (Fig. S2 H), suggesting a disruption in SLCF-1 exocytosis and potential redirection for degradation. We further employed apically localized ERM-1 and NHX-2 as representative cargos (Wang et al., 2021). ERM-1 and NHX-2 labeling on the apical membrane was unaffected by the loss of RAB-10 and EHBP-1 (Fig. S2, I–J′). Together, these findings suggest a general involvement of RAB-10 and EHBP-1 in basolateral exocytosis.

In both HepG2 cells and worm intestines, our research found that the absence of RAB-10/Rab10 impeded exocytosis, which could ultimately lead to cargo degradation. To consolidate this assessment, Rab10 knockdown cell lines were generated in Huh7 cells. Indeed, the loss of Rab10 decreased apoB levels in both intracellular and extracellular fractions without significant changes in apoB mRNA levels (Fig. S2, K and K′; and Table S2). The introduction of the lysosome inhibitor bafilomycin A1 led to a notable recovery in the intracellular levels of apoB in Rab10-deficient cells with a less pronounced impact observed for the proteasome inhibitor MG132 treatment (Fig. S2, K and K′). Likewise, in *rab-10* and *ehbp-1* mutants, further knockdown of the lysosomal V-ATPase components VHA-1 and VHA-2 (Li et al., 2023), as well as RAB-7, resulted in a prominent recovery in both the quantity and intensity of SLCF-1-labeled structures (Fig. S2, L and L′). We additionally examined the colocalization between VIT-2 and either the TGN marker mCherry-GOLG-4 or the lysosome marker LAAT-1-mCherry. A minimal degree of overlap between VIT-2 and GOLG-4 was observed, unaffected by the absence of RAB-10 and EHBP-1 (Fig. S2, M and M′). However, a significant increase in VIT-2 colocalization with LAAT-1 was noted in both *rab-10* and *ehbp-1* mutants (Fig. S2, N and N′). These findings collectively suggest that the control of lipoprotein export from the Golgi is not contingent on RAB-10 and EHBP-1. Their deficiency is likely to cause a buildup of exocytic cargos in endosomes rather than the Golgi, ultimately leading to lysosomal degradation.

RAB-10/EHBP-1 facilitates lipoprotein exocytic delivery toward recycling endosomes

In the *C. elegans* intestine, EHBP-1 is located in the recycling endosomal meshwork, where it collaborates with RAB-10 to regulate basolateral recycling (Shi et al., 2010; Wang et al., 2016; Gao et al., 2020). This functional attribute of EHBP-1 and RAB-10 raises questions about the involvement of the endosomal recycling system in basolateral exocytosis. To address this query, we examined the colocalization of recycling regulators with VIT-2. We focused on CED-10 and LET-413, which are located in both

early and recycling endosomes, and RME-1, which is mainly situated in recycling endosomes (Sun et al., 2012; Liu et al., 2018). The data indicated that VIT-2-labeled structures were often found within structures labeled with CED-10 and LET-413 (Fig. 2, A, B, and E). Also, VIT-2 displayed partial overlap with RME-1 and was frequently located in punctate regions within the tubulated endosomal network (Fig. 2, C and E). It is noteworthy that the recycling cargo hTAC labels the endosomal network that governs recycling more extensively than individual regulators. We also observed significant colocalization of VIT-2 with hTAC in punctate and tubular structures (Fig. 2, D and E). Together, these results suggest the involvement of the endosomal recycling system in basolateral exocytic trafficking.

Prior studies in *C. elegans* have identified ARF-6, AMPH-1, LET-502, PTRN-1, RME-1, RTKN-1, SDPN-1, CED-10, LET-413, and SID-3 as involved in regulating basolateral recycling (Chen et al., 2018; Gong et al., 2018; Gao et al., 2020; Zhang et al., 2020, 2023; Yan et al., 2021; Grant et al., 2001; Pant et al., 2009; Liu et al., 2018). In RME-1-deficient animals, we noticed an increased basolateral presence of VIT-2 and decreased VIT-2 levels within oocytes (Fig. 2 F and Fig. S3 B). However, unlike the RAB-10 deficiency phenotype, in *rme-1* mutants, VIT-2 was commonly observed within enlarged structures and vacuoles (Fig. 2 G), attributed to the aberrant fusion of recycling endosomes (Lin et al., 2001; Chen et al., 2006). Upon LET-413 depletion, a similar phenotype manifested, with VIT-2 accumulating in the intestine and yolk aggregating in the body cavity, potentially due to impaired oocyte endocytosis (Fig. 2, F–G′ and Fig. S3 B). In contrast, depletion of ARF-6, AMPH-1, LET-502, PTRN-1, RTKN-1, SDPN-1, CED-10, and SID-3 did not affect the distribution of VIT-2 across tissues (Fig. 2 F and Fig. S3 B).

The interaction between EHBP-1/EHBP1 and RME-1/EHDs is not conserved in *C. elegans* (Shi et al., 2010). To determine the functional relationship between RME-1, LET-413, and either RAB-10 or EHBP-1, a genetic analysis was performed. In *rme-1(b1045)* mutants, depletion of either RAB-10 or EHBP-1 led to a decrease in basolateral VIT-2 and cytosolic accumulation of VIT-2, resembling the phenotype of *rab-10* or *ehbp-1* mutants (Fig. 2, G and G′). LET-413 holds a functional position similar to RME-1, situated downstream of RAB-10 and EHBP-1 (Fig. 2, G and G′). Then, we utilized a PI(4,5)P2 reporter, Tubby-PH^{R332H}, to visualize recycling endosomes and basolateral membrane. The *rab-10* and *ehbp-1* mutants exhibited a reduced overlap of VIT-2 with Tubby-PH^{R332H} (Fig. 2, H and H′), indicating impaired exocytic transport to recycling endosomes and the plasma membrane. In contrast, in *rme-1(b1045)* and *let-413*(RNAi) animals, we observed extensive accumulation of VIT-2 in Tubby-PH^{R332H}-positive structures and vacuoles (Fig. 2, H and H′). Together, these observations suggest that RAB-10 and EHBP-1 promote exocytic trafficking toward recycling endosomes, followed by the involvement of RME-1 and LET-413.

Loss of EHBP-1 leads to increased dynamics of RAB-10-labeled exocytic carriers

To better understand the interplay between RAB-10 and EHBP-1 in regulating basolateral exocytosis, we assessed the effect of overexpressing RAB-10 and/or EHBP-1 on the distribution of VIT-2. Interestingly, co-overexpression of RAB-10 and EHBP-1 led to an enlargement of VIT-2-labeled structures where both proteins were localized on the surface (Fig. 3, A–B′), suggesting a collaborative role of EHBP-1 and RAB-10 in modulating the morphology of exocytic carriers. Next, we tagged the endogenous RAB-10 (wrmScarlet-3xFlag-RAB-10) and observed a partial overlap between RAB-10 and VIT-2, which was more pronounced in the absence of EHBP-1 (Fig. 3, C and C′). To improve the image quality, we created a single-copy knock-in allele, EHBP-1-mCherry^{SC}. Notably, the lack of RAB-10 led to a significant reduction in the colocalization of VIT-2 with EHBP-1 (Fig. 3, D and D′), suggesting that RAB-10 acts upstream of EHBP-1 in the exocytic pathway.

It should be noted that in cells lacking EHBP-1, VIT-2 is found on smaller structures, which RAB-10 frequently labels (Fig. 1 B and Fig. 3 C). To delineate this phenotype, we examined the effects of EHBP-1 deficiency on both endogenous and transgenic RAB-10. In *ehbp-1* mutants, RAB-10-labeled structures appeared as numerous small puncta (Fig. 3, E–E″ and Fig. S4, A–A″); however, the loss of EHBP-1 did not affect the RAB-10 membrane-to-cytosol ratio (Fig. S4 B), indicating unchanged RAB-10 activity (Liu et al., 2018). Then, we performed live-cell imaging of RAB-10-labeled structures. In wild-type animals, these structures showed a dynamic movement toward neighboring structures, leading to convergence. In the absence of EHBP-1, these structures tended to undergo more fission events while maintaining a consistent merging frequency (Fig. 3 F; and Videos 1 and 2).

EHBP-1 facilitates the convergence of RAB-10-positive carriers toward recycling endosomes

Homotypic fusion commonly exists in the endosomal system (Simonsen et al., 1998). To examine whether it occurs between RAB-10-labeled carriers, we fused a mitochondrial localization signal (Mito) to the N-terminus of RAB-10 (Upadhyay et al., 2008), resulting in its redirection to mitochondria costained with hMAOA-CT (Wong and Munro, 2014) (Fig. S4, C and C′). A significant overlap was observed between endogenous and mitochondria-located RAB-10, which was unaffected in *ehbp-1* mutants (Fig. 4, A and A′). Consistently, in the presence of Mito-mCherry-RAB-10, there was a substantial increase in mitochondrial VIT-2. The absence of EHBP-1 did not impact this relocation (Fig. 4, B and B′). EHBP-1 is commonly present in a network of tubular recycling endosomes (Shi et al., 2010; Wang et al., 2016; Gao et al., 2020). In the absence of EHBP-1, there was an increase in the number of RAB-10-labeled structures, accompanied by a decrease in their proximity to Tubby-PH^{R332H}-labeled recycling endosomes (Fig. 4, C and C′). In contrast, an increase in the colocalization of RAB-10 and Tubby-PH^{R332H} was observed in cells overexpressing EHBP-1. These findings suggest that, although EHBP-1 is dispensable for homotypic clustering of RAB-10-labeled lipoprotein exocytic carriers, it contributes to their convergence toward recycling endosomes.

To validate this notion, we conjugated the nanobody RFPnb, which specifically binds to mCherry, to the N-terminus of RAB-10. Moreover, we employed DHS-3-mCherry to label lipid droplets, facilitating the relocation of RAB-10 to these organelles

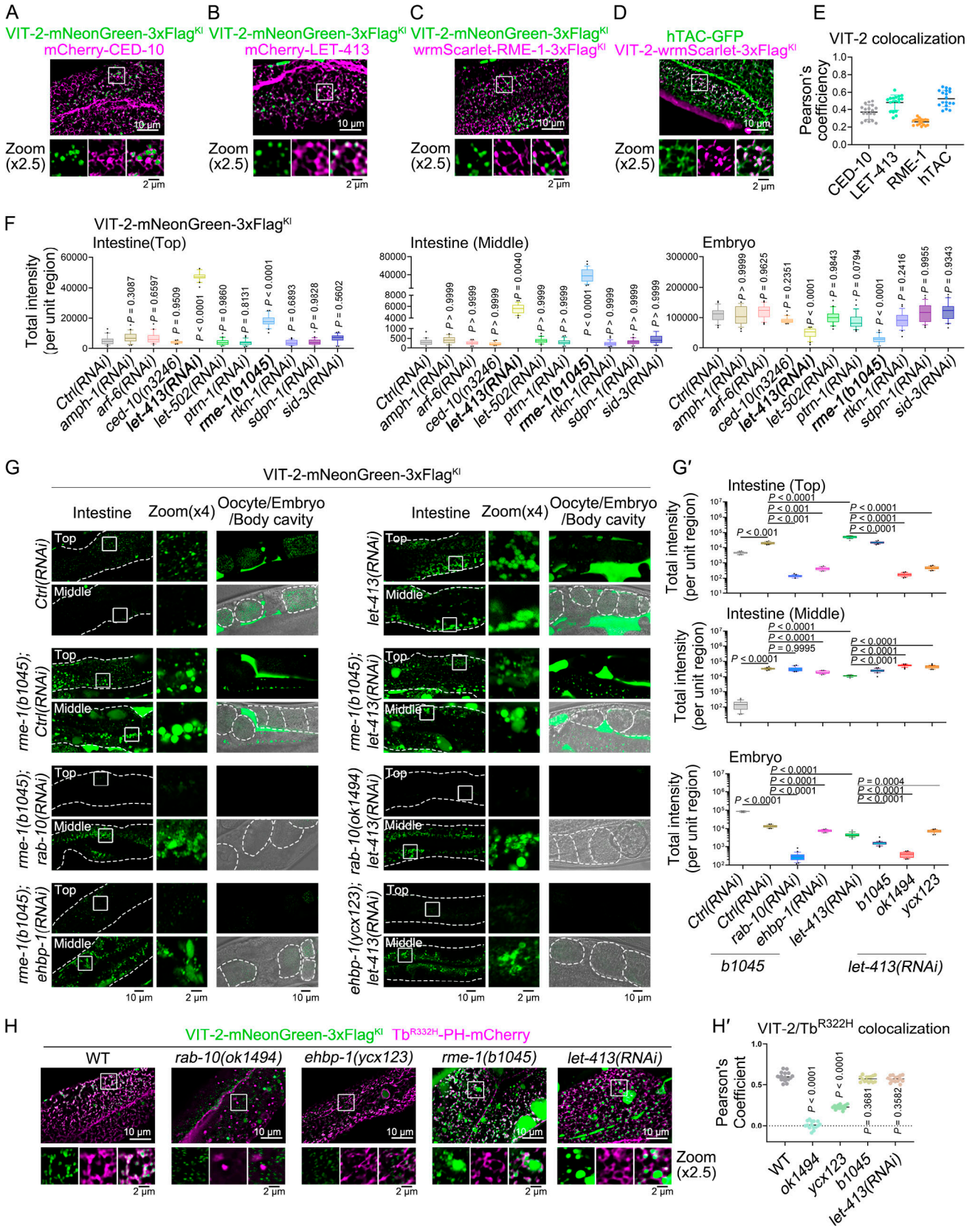

Figure 2. **The recycling regulators RME-1 and LET-413 function in the basolateral exocytic trafficking pathway, operating downstream of RAB-10 and EHBP-1. (A–E)** Confocal images showing colocalization between VIT-2 and CED-10, LET-413, RME-1, or hTAC. Statistical analysis of colocalization was calculated as Pearson's correlation coefficient and is shown as the mean ± SD (n = 18 cells from six animals of each genotype). **(F)** The intensity of VIT-2-mNeonGreen-3xFlag^{KI}-labeled structures in the intestinal top, middle, or embryos was measured after RNAi-mediated knockdown of various endocytic

recycling regulators. The data are shown as box-and-whisker plots with 10th–90th percentile (n = 24 cells from eight animals of each genotype; dots, outliers; boundaries, quartiles; one-way ANOVA test with Dunn's multiple comparison). **(G and G′)** Confocal images showing the distribution of VIT-2-mNeonGreen-3xFlag^{KI} in the *C. elegans* intestine, oocytes, and embryos. White dashed lines indicate the outlines of the intestine, oocytes, or embryos. The data are shown as box-and-whisker plots with 10th–90th percentile (n = 24 cells from eight animals of each genotype; dots, outliers; boundaries, quartiles; two-way ANOVA with Bonferroni post-test). **(H and H′)** Confocal images showing colocalization between VIT-2-mNeonGreen-3xFlag^{KI} and Tubby-PH^{R332H}-mCherry in different genetic backgrounds. Statistical analysis of colocalization was calculated as Pearson's correlation coefficient and is shown as the mean ± SD (n = 18 cells from six animals of each genotype, one-way ANOVA test with Dunn's multiple comparison).

(Fig. 4 D). In the wild-type background, there was no colocalization between Tubby-PH^{R332H}-labeled endosome and DHS-3-mCherry-marked lipid droplet, and this pattern remains unaffected by EHBP-1 overexpression (Fig. 4, E and E′). However, the introduction of RFPnb-RAB-10 induced a convergence between two organelles, which was abolished in the absence of EHBP-1 (Fig. 4, E and E′). This colocalization was enhanced upon overexpression of EHBP-1-BFP (Fig. 4, E and E′), underscoring the role of EHBP-1 in promoting the convergence of RAB-10-labeled carriers toward recycling endosomes and the significance of RAB-10 in this mechanism.

EHBP-1 sequesters lipoprotein exocytic carriers in a mechanism that relies on the functionality of RAB-10

The CC tether EEA1 directs Rab5-associated vesicles toward the target membrane (Murray et al., 2016). This prompts an inquiry into whether there are resemblances in the functional mode of RAB-10 and EHBP-1. EHBP-1's residence at recycling endosome depends on PI(4,5)P2 binding by its C2-like domain, which can be disrupted by specific mutations (RRLRR6AALAA) (Wang et al., 2016). By adding a Mito signal at the N-terminus, EHBP-1^{6AALAA} was redirected to the mitochondria labeled with hMAOA-CT (Fig. 5 A; and Fig. S4, D and D′). Of note, while VIT-2 did not colocalize with Mito-mCherry, the overexpression of Mito-EHBP-1^{6AALAA} resulted in the translocation of VIT-2 to the mitochondria (Fig. 5, B and B′). In the absence of RAB-10, the localization of VIT-2 in mitochondria was reduced (Fig. 5, B and B′). In contrast, overexpressing RAB-10 led to an elevated level of mitochondrial VIT-2 (Fig. 5, B and B′). Consistently, TEM revealed a clustering of yolk vesicles near mitochondria upon overexpression of Mito-EHBP-1^{6AALAA}, with this observation being reliant on the existence of RAB-10 (Fig. 5 C). Importantly, we noticed that the mitochondrial targeting of VIT-2 was specifically induced by the overexpression of active RAB-10(Q68L) rather than inactive RAB-10(T23N) (Fig. 5, B and B′). Hence, our findings suggest a model in which EHBP-1 potentially acts as a tether, facilitating the proximity of yolk exocytic vesicles to their target compartments, with this mechanism requiring the presence of active RAB-10.

Likewise, a GFP nanobody (GFPnb) was fused to the N-terminus of EHBP1 without the C2 domain, and the relocation of EHBP1 to the lipid droplet was facilitated using GFP-PLIN2 (Fig. 5, D and D′). In HepG2 cells, apoB-labeled vesicles did not colocalize with lipid droplets. Notably, in cells overexpressing GFPnb-EHBP1(ΔC2), apoB showed significant overlap with GFP-PLIN2 (Fig. 5, D and D′). Co-overexpression of Rab10 and GFPnb-EHBP1(ΔC2) further enhanced this colocalization (Fig. 5, D and D′), indicating the conserved role of EHBP1 and Rab10 in capturing lipoprotein exocytic carriers.

To directly evaluate the carriers' capturing capacity mediated by EHBP-1 and RAB-10, a liposome tethering assay was performed. The non-specific binding of EHBP-1 to liposomes was minimized by utilizing a truncated EHBP-1 that lacked the C2 domain and instead included a StrepII tag at the N-terminus. EHBP-1ΔC2 was immobilized on a Biotin PEG-coated slide, and its efficiency in capturing fluorescent liposomes was evaluated using TIRF imaging (Fig. 5 E). Upon introducing the GTP analogy GMP-PNP-loaded RAB-10, which contains a His-tag for affinity toward liposomes, an increase in fluorescence intensity was observed, signifying liposome capture (Fig. 5, F and F′). The capturing efficiency further improved with higher concentrations of EHBP-1, plateauing at 1 μM (Fig. S4, E and E′). To investigate the role of the RAB-10–EHBP-1 interaction in this process, the CC domain of EHBP-1, crucial for RAB-10 binding, was further deleted. No significant alterations in intensity were noted on the slides immobilized with EHBP-1(ΔC2 ΔCC) following the introduction of GMP–PNP–loaded RAB-10 (Fig. 5, F and F′), indicating that liposome capture is contingent upon the interaction between RAB-10 and EHBP-1.

To assess whether EHBP-1's ability to capture vesicles is involved in recycling, we examined the distribution of the recycling cargo hTAC-GFP. However, hTAC-GFP did not relocate to the mitochondria in cells overexpressing Mito-mCherry-RAB-10 or Mito-EHBP-1^{6AALAA}-mCherry (Fig. S4, F and F′), suggesting that EHBP-1-assisted vesicular carrier sequestration is not implicated in the exocytosis of hTAC and its basolateral recycling.

Lipoprotein exocytic carrier sequestration is contingent upon the binding capabilities of EHBP-1 to RAB-10 and PI(4,5)P2

The CC domain of EHBP-1 plays a role in interacting with active RAB-10, while its N-terminal C2-like domain is responsible for interacting with PI(4,5)P2, and its central CH domain interacts with F-actin (Wang et al., 2016). The interaction interface between EHBP-1 and the active RAB-10(Q68L) was validated using AlphaFold2-Multimer (Fig. 6 A). We generated transgenic strains expressing mitochondria-targeted EHBP-1 variants lacking the C2-like, CH, and CC domains, respectively. Upon expression of Mito-ΔC2, VIT-2 translocated to the mitochondria (Fig. 6, B–C′). Similarly, the presence of Mito-ΔCH^{6AALAA} led to mitochondrial localization of VIT-2, albeit to a lesser extent (Fig. 6, B–C′). Instead, the introduction of Mito-ΔCC^{6AALAA} failed to relocate VIT-2 to the mitochondria (Fig. 6, B–C′). These results highlight EHBP-1's reliance on its interaction with RAB-10 to capture exocytic vesicles, while also hinting at the impact of the CH domain–mediated actin binding on this process.

The N-terminus of α-actinin consists of a Type 1 CH domain (CH1) and a Type 2 CH domain (CH2). CH1 exhibits an ∼10-fold

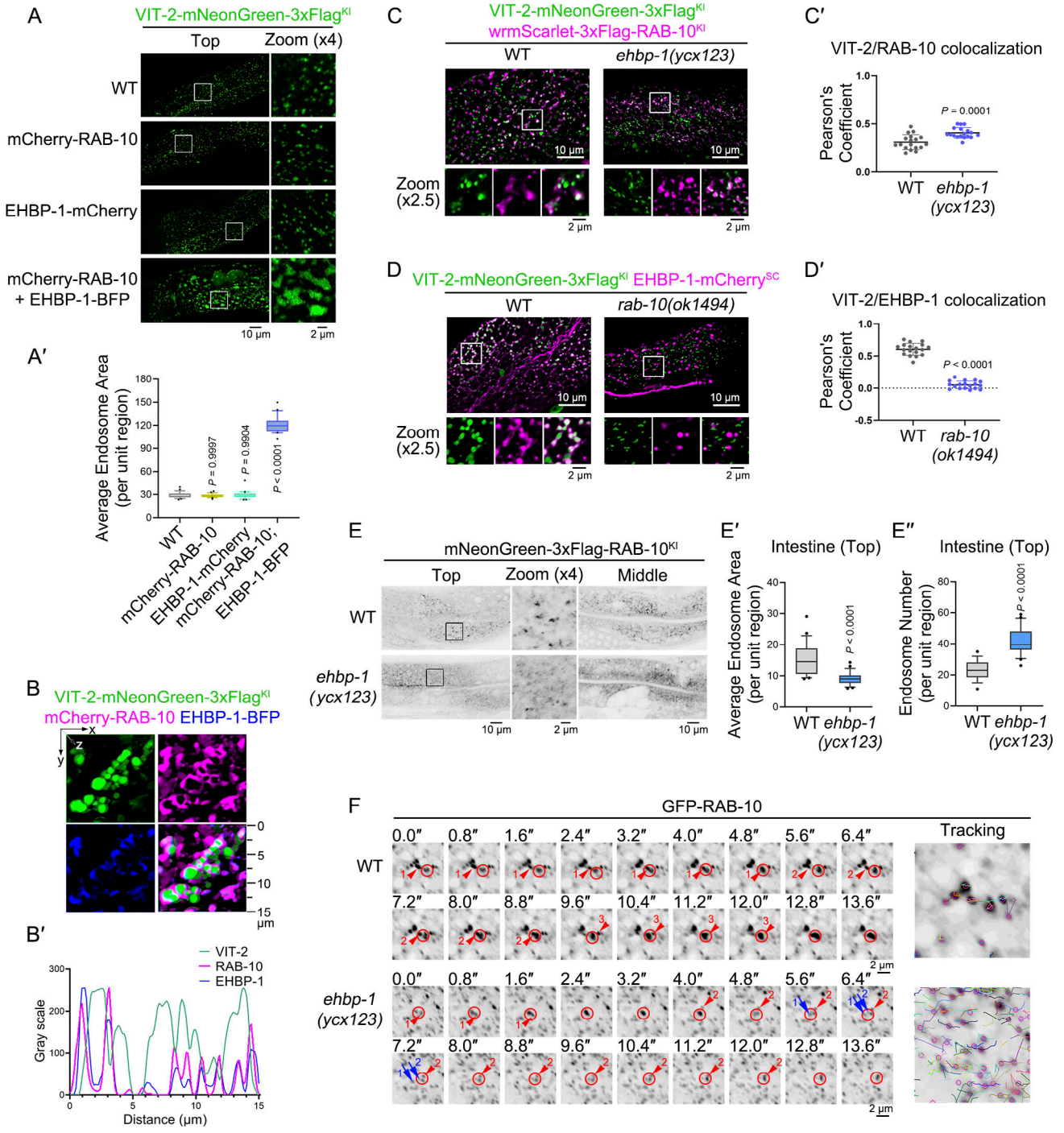

Figure 3. **Loss of EHBP-1 leads to increased dynamics in RAB-10-labeled exocytic carriers. (A and A′)** Confocal images showing the morphology of endogenous VIT-2-associated endosome (VIT-2-mNeonGreen-3xFlag^{KI}) in different genetic backgrounds. The data are shown as box-and-whisker plots with 10th–90th percentile (n = 24 cells from eight animals of each genotype; dots, outliers; boundaries, quartiles; one-way ANOVA test with Dunn's multiple comparison). **(B and B′)** Volume confocal images showing colocalization between VIT-2-mNeonGreen-3xFlag^{KI}, mCherry-RAB-10, and EHBP-1-BFP. Line scan profiles of the three channels of the white line were conducted using ImageJ. **(C and C′)** Confocal images showing colocalization between VIT-2-mNeonGreen-3xFlag^{KI} and wrmScarlet-3xFlag-RAB-10^{KI} in different genetic backgrounds. **(D and D′)** Confocal images showing colocalization between VIT-2-mNeonGreen-3xFlag^{KI} and EHBP-1-mCherry^{SC} in different genetic backgrounds. Statistical analysis of colocalization was calculated as Pearson's correlation coefficient and is shown as the mean ± SD (n = 18 cells from six animals of each genotype; two-tailed Mann-Whitney test). **(E–E″)** Confocal images showing the morphology of endogenous RAB-10-associated endosome (mNeonGreen-3xFlag-RAB-10^{KI}). Statistical data is shown as box-and-whisker plots with 10th–90th percentile (n = 24 cells from eight animals of each genotype; dots, outliers; boundaries, quartiles; two-tailed Mann-Whitney test). **(F)** Spanning disk confocal images showing the dynamics of GFP-RAB-10-labeled endosomes. Red arrowheads represent the movement of RAB-10-associated structures toward neighboring structures, resulting in eventual convergence. Green arrowheads illustrate fission events within RAB-10-associated structures. The moving routes were tracked using TrackMate. The tiny rings indicate the endosomal structures, while the zigzag lines indicate the dynamic trajectory of these structures.

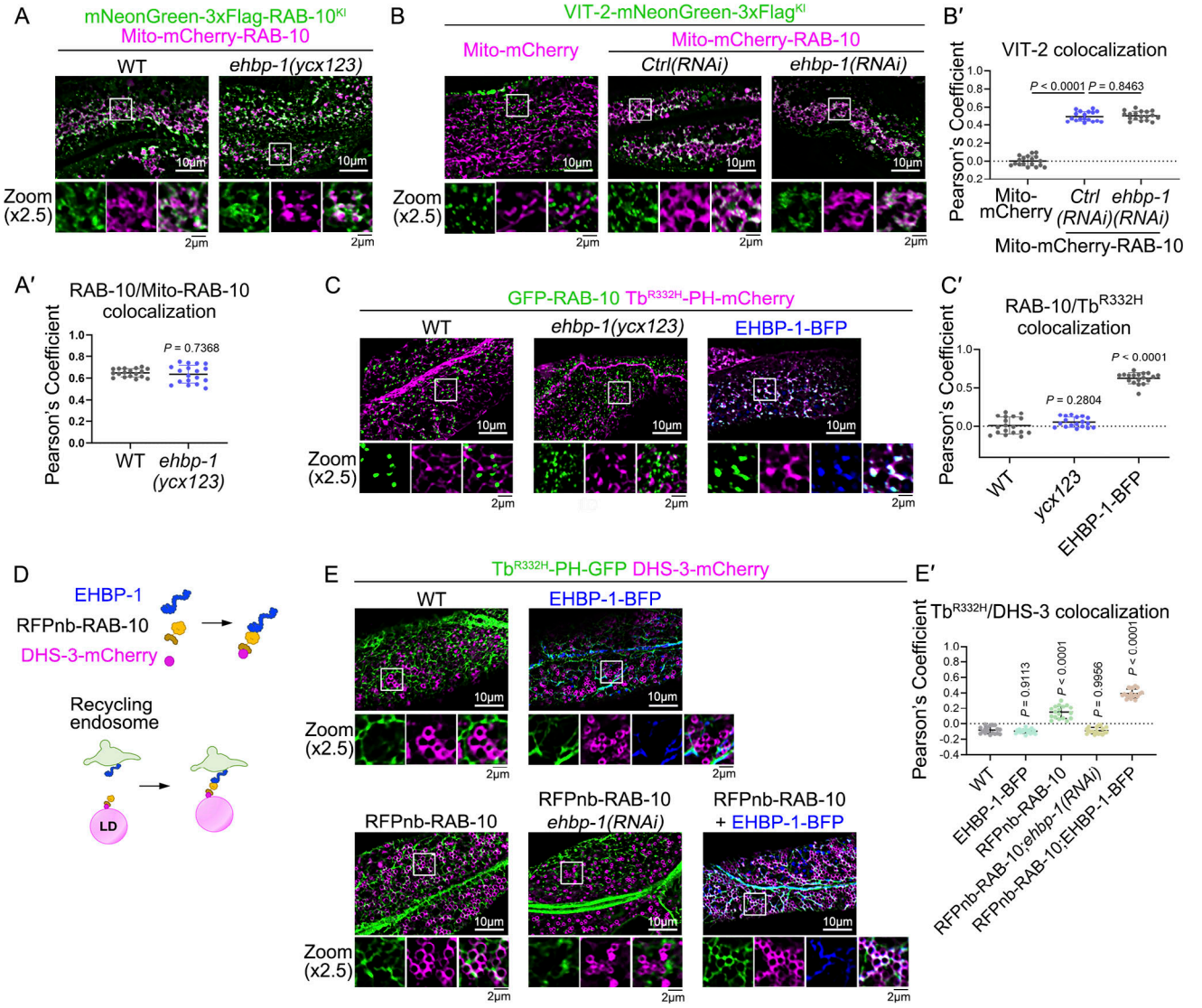

Figure 4. **EHBP-1 contributes to the sequestration of RAB-10-associated endosomes onto recycling endosomes. (A and A′)** Confocal images showing colocalization between mNeonGreen-3xFlag-RAB-10^{KI} and Mito-mCherry-RAB-10. **(B and B′)** Confocal images showing colocalization between VIT-2-mNeonGreen-3xFlag^{KI} and mitochondria in different genetic backgrounds. **(C and C′)** Confocal images showing colocalization between GFP-RAB-10 and Tubby-PH^{R332H}-mCherry. **(D)** Cartoon picture showing the working model of RFPnb-mediated protein translocation. **(E and E′)** Confocal images showing colocalization between Tubby-PH^{R332H}-GFP and DHS-3-mCherry. The statistical analysis of colocalization was calculated as Pearson's correlation coefficient and is shown as the mean ± SD (n = 18 cells from six animals of each genotype; one-way ANOVA test with Dunn's multiple comparison in B′, C′, and E′; two-tailed Mann–Whitney test in A′).

lower affinity for F-actin compared with the full actin-binding region encompassing both CH domains, while CH2 lacks actin-binding activity (Way et al., 1992; Gimona et al., 2002; Winder et al., 1995). To assess the effect of EHBP-1's actin-binding ability on the capture of lipoprotein carriers, we prepared a hybrid EHBP-1 construct by replacing its CH domain with the CH2 domain of human α-actinin. Despite the prediction that this variant would not bind to F-actin, VIT-2 was still translocated to the mitochondria (Fig. 6, B–C′), suggesting that EHBP-1's actin-binding capacity is not essential for facilitating the sequestration of exocytic carriers.

Additionally, we examined whether the yolk exocytic defects could be alleviated by overexpressing these EHBP-1 variants. We developed a strain to express endogenous EHBP-1 tagged with 7xGFP11 and then used RNAi to selectively suppress 7xGFP11, causing the downregulation of EHBP-1 (Fig. 6, D–E′). In *7xgfp11(RNAi)* animals, VIT-2 exhibited accumulation in the intestine and reduction in the oocytes. EHBP-1–mCherry effectively rescued these defects, whereas EHBP-1(ΔC2) and EHBP-1(ΔCC) failed to do so (Fig. 6, E and E′). Of note, EHBP-1(ΔCH) partially reinstated the VIT-2 distribution in both the intestine and oocytes (Fig. 6, E and E′). Similarly, the distribution defect of VIT-2 was alleviated by overexpressing EHBP-1 variants containing α-actinin CH1-CH2 or CH2 (Fig. 6, E and E′). EHBP-1 variants with α-actinin CH1 also mitigated the secretion defect of VIT-2, albeit with slightly less efficacy, as evidenced by residual VIT-2 accumulation in the

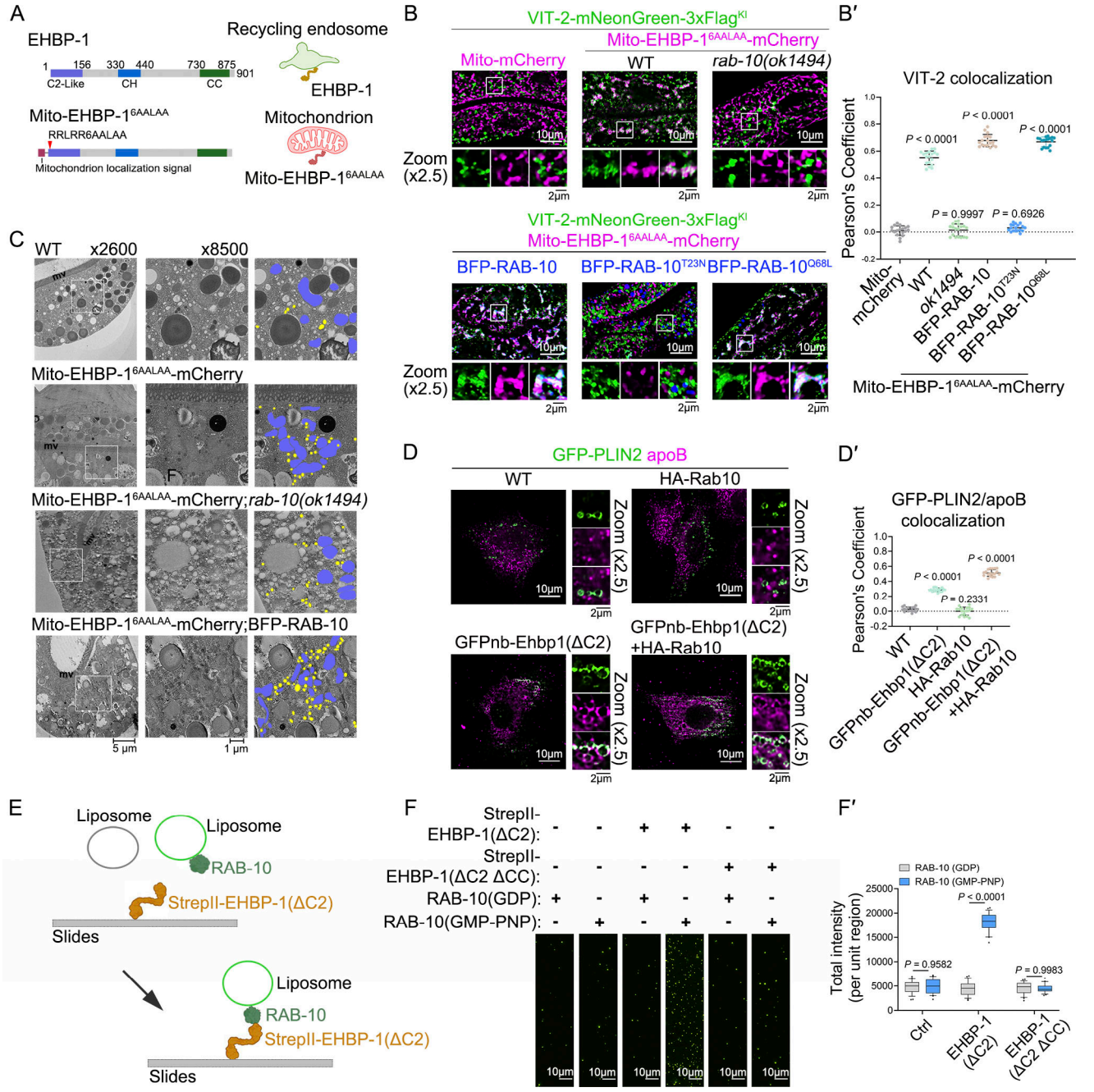

Figure 5. **Exocytic carrier sequestration by EHBP-1 depends on RAB-10 functionality. (A)** Domain architecture and subcellular localization of EHBP-1 and Mito-EHBP-1^{6AALAA}. **(B and B′)** Confocal images showing colocalization between VIT-2-mNeonGreen-3xFlag^{KI} and mitochondria. Statistical analysis of co-localization was calculated as Pearson's correlation coefficient and is shown as the mean ± SD (n = 18 cells from six animals of each genotype; one-way ANOVA test with Dunn's multiple comparison). **(C)** TEM images showing the spatial relationship between the yolk and the mitochondria. Yellow and blue indicate the yolk and the mitochondria, respectively. **(D and D′)** Confocal images showing colocalization between GFP-PLIN2-labeled lipid droplets and lipoproteins in HepG2 cells. Statistical analysis was calculated as Pearson's correlation coefficient and is shown as the mean ± SD (n = 18 cells; one-way ANOVA test with Dunn's multiple comparison). **(E)** Cartoon image showing the liposome tethering assay. **(F and F′)** The images acquired using a TIRF microscope showing liposomes equipped with RAB-10(GMP-PNP) or RAB-10(GDP) captured by slides immobilized with StrepII-EHBP-1(ΔC2) or StrepII-EHBP-1(ΔC2 ΔCC). Statistical data are shown as box-and-whisker plots with the 10th–90th percentile (n = 24 areas; dots, outliers; boundaries, quartiles; two-way ANOVA with Bonferroni post-test).

intestinal cytosol (Fig. 6, E and E′). These findings support that EHBP-1 regulates basolateral exocytosis independently of F-actin binding. The diminished efficacy of EHBP-1(ΔCH) in rectifying defects in exocytic carrier sequestration and yolk secretion could be attributed to structural changes. Together, our results highlight the significance of EHBP-1's C2 domain for associating with recycling endosomes and its CC domain for interacting with exocytic carrier-located RAB-10 during basolateral lipoprotein exocytosis.

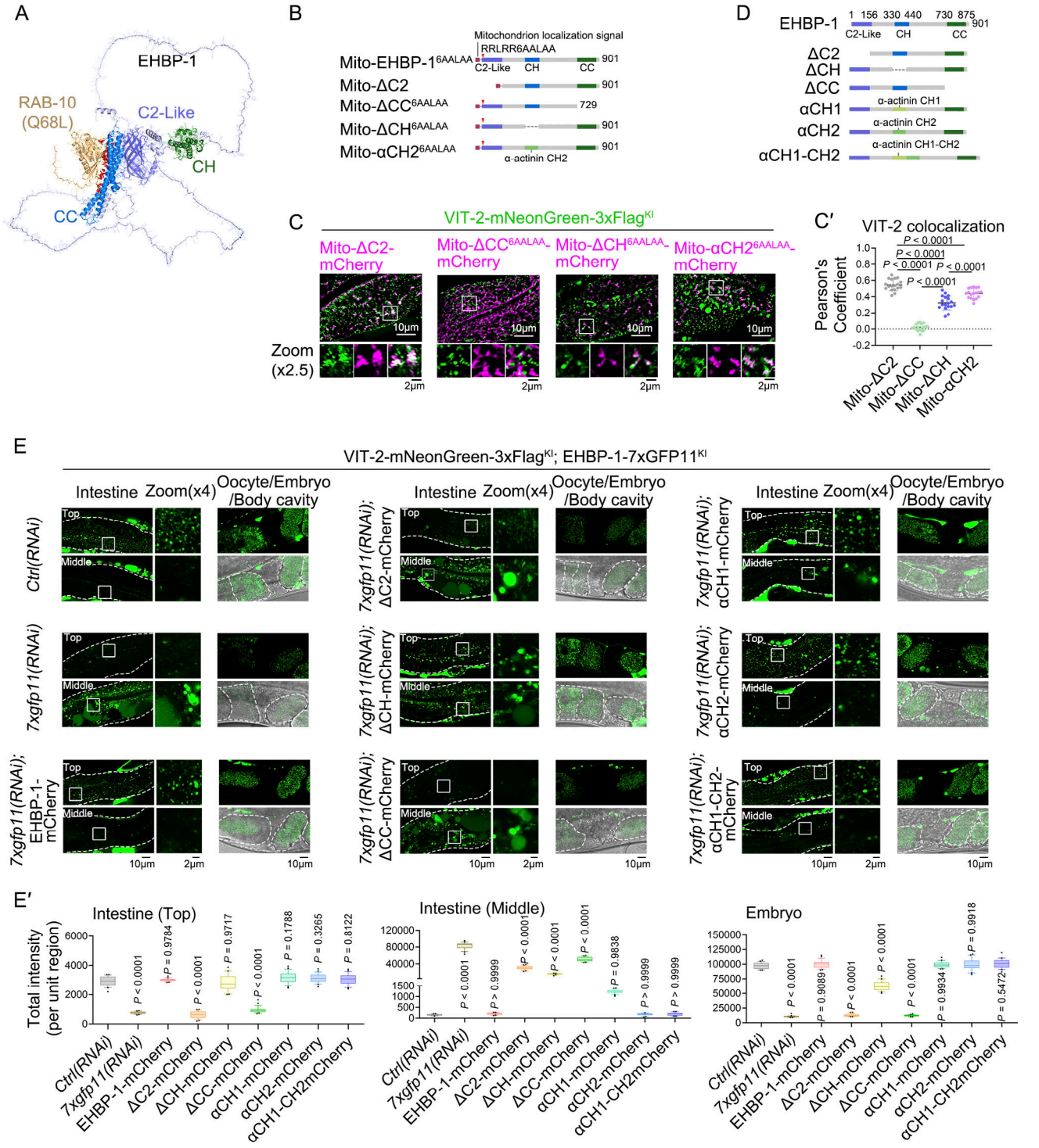

Figure 6. **Exocytic carrier sequestration relies on EHBP-1's binding to RAB-10 and PI(4,5)P2. (A)** The interaction between EHBP-1 and RAB-10(Q68L) predicted by AlphaFold2-Multimer. Red sticks indicate contacts between EHBP-1 and RAB-10(Q68L) within 4.0 Å. **(B)** Cartoon image showing domain architectures of Mito-EHBP-1^{6AALAA}, Mito-ΔC2, Mito-ΔCC^{6AALAA}, Mito-ΔCH^{6AALAA}, and Mito-αCH2^{6AALAA}. **(C and C′)** Confocal images showing colocalization between VIT-2-mNeonGreen-3xFlag^{KI} and mitochondria. The statistical analysis was calculated as Pearson's correlation coefficient and shown as mean ± SD (n = 18 cells from six animals of each genotype; one-way ANOVA test with Dunn's multiple comparison). **(D)** Cartoon image showing domain architecture of EHBP-1 truncation and domain substitution variants. **(E and E′)** Confocal images showing the distribution of VIT-2-mNeonGreen-3xFlag^{KI} in the *C. elegans* intestine, oocytes, and embryos in different gene knockdown backgrounds. Statistical data are shown as box-and-whisker plots with 10th–90th percentile (n = 24 cells from eight animals of each genotype; dots, outliers; boundaries, quartiles; one-way ANOVA test with Dunn's multiple comparison).

LST-6/DENND5 serves as a GEF for RAB-10 in lipoprotein exocytic transport

In basolateral recycling, the activation of RAB-10 is regulated by the GEF protein DENN-4/DENND4 (Liu et al., 2018; Zhang et al., 2023). To identify the GEF for activating RAB-10 in post-Golgi exocytic trafficking, we studied putative RAB-10/Rab10 GEFs, UNC-73/TRIO, and DENN-4 (Tao et al., 2019; Liu et al., 2018), as well as LST-6/DENND5 (R6IP1) (Miserey-Lenkei et al., 2007; Fernandes et al., 2009), the sole paralog of DENN-4. No significant changes were observed in the distribution of VIT-2 in *denn-4(RNAi)* and *unc-73(RNAi)* animals (Fig. 7, A and A′). On the contrary, the loss of LST-6 led to an intracellular buildup in the intestine along with reduced VIT-2 levels in oocytes (Fig. 7, A and A′). Furthermore, in the absence of LST-6, there was a reduction in the number and intensity of RAB-10-positive puncta (Fig. 7, B and B′), suggesting compromised RAB-10 activity. We then evaluated the changes in RAB-10 activity through a membrane fractionation assay (Liu and Grant, 2015; Liu et al., 2018). Accordingly, we observed a decrease in the membrane-to-cytosol ratio of RAB-10 (from ∼2.1 to ∼0.7: $n = 3$ replicates) (Fig. 7, C and C′), signifying a reduction in RAB-10 activity following the loss of LST-6. In addition, we prepared a single-copy knock-in allele, LST-6::GFP^{SC}. Notably, we observed the frequent presence of LST-6 on punctate structures labeled by RAB-10 (Fig. S5, A and A′). Previous studies have indicated that DENN-4 primarily localizes to meshwork-like recycling endosomes (Zhang et al., 2023; Liu et al., 2018). Indeed, our data revealed minimal colocalization between LST-6 and DENN-4 (Fig. S5, B and B′), suggesting that LST-6 and DENN-4 are located on distinct endosomal structures, serving as RAB-10-GEFs that regulate secretion and recycling transport, respectively.

To determine LST-6's specificity for Rabs in endosomal trafficking, we examined its interaction with Rab mutants, including the constitutively active forms RAB-10(Q68L), RAB-7(Q68L), RAB-8(Q67L), and RAB-11.1(Q70L), as well as the GDP-bound mutants RAB-10(T23N), RAB-7(T23N), RAB-8(T22N), and RAB-11.1(S25N). Of note, LST-6 interacts with inactive RAB-10(T23N) (Fig. 7 D). In line with the function of a GEF, the DENN domain of LST-6 exhibited a binding affinity toward RAB-10(T23N) (Fig. 7 E). Also, we noticed that LST-6 displayed binding to both RAB-8(T22N) and RAB-11.1(S25N) (Fig. 7 D), suggesting its possible involvement in the regulation of apical recycling (Sato et al., 2014; Casanova et al., 1999).

Previous investigation revealed an autoinhibitory conformation of DENN-4 (Liu et al., 2018). Therefore, we assessed the GEF activity of the DENN domains in LST-6 and DENN-4, as well as the full-length LST-6 toward RAB-10, and determined the rate constants (k) for each using nonlinear regression (curve fit) (Fig. 7 F and Fig. S5, C–G). The k value of LST-6 is higher than that of LST-6-DENN and DENN-4-DENN. These results suggest that LST-6 may not assume a self-inhibitory conformation. Then, we investigated the GEF activity of LST-6 toward RAB-8 and RAB-11.1. LST-6 exhibits moderate GEF activity toward RAB-8, while showing almost no GEF activity toward RAB-11.1 (Fig. 7 F and Fig. S5, F and G). However, knocking down LST-6 had almost no effect on the distribution of RAB-8 and RAB-11.1, suggesting that in vivo, LST-6 may not specifically act on RAB-8 and RAB-11.1 (Fig. S5, D–E′). To assay the effect of LST-6 on RAB-10 in vivo, the colocalization between VIT-2 and Mito-EHBP-1^{6AALAA} was examined. In cells lacking LST-6, the presence of VIT-2 in mitochondria was remarkably reduced (Fig. 7, G and G′). In contrast, the loss of LST-6 did not affect the distribution of the recycling cargo hTAC-GFP (Fig. S5, J and J′). We also examined the regulatory role of the mammalian homolog of LST-6. Given the inefficacy of the knockdown of DENND5A/B in HepG2 cells, we opted to create shRNA-mediated knockdowns of DENND5A and DENND5B in Huh7 cells (Fig. S5, K and L). Following DENND5A/B knockdown, there was a significant decrease in apoB levels in both the supernatant and intracellular fractions (Fig. 7, H–H″), with no alteration in expression (Fig. S5, M and N), consistent with the findings from Rab10 knockdown. Together, these findings indicate LST-6/DENND5's role in regulating lipoprotein exocytic transport across species. Also, our data suggest the involvement of different RAB-10-GEFs in distinct trafficking pathways, with LST-6 specifically acting in basolateral exocytosis.

RAB-10 and EHBP-1 regulate basolateral exocytosis upstream of the exocyst complex

In yeast, the exocyst complex acts as a tether, promoting the fusion of secretory vesicles with the plasma membrane by interacting with Rab10/Sec4 (Guo et al., 1999). Also, there is evidence indicating that Rab10 works with the exocyst to regulate ciliogenesis in MDCK cells (Babbey et al., 2010). Thus far, our results suggest that EHBP-1 could serve as a tether for exocytic carriers. To elucidate the relationship between the exocyst and RAB-10–EHBP-1, we utilized RNAi to deplete exocyst components and assessed the impact on VIT-2 distribution. Our results were classified into three groups: Group 1 (SEC-3, SEC-10, SEC-15, and EXOC-7) had no impact on VIT-2 distribution; Group 2 (SEC-6 and EXOC-8) showed reduced levels in oocytes and embryos; Group 3 (SEC-5 and SEC-8) led to VIT-2 accumulation in intestinal cells. Of note, deficiency in SEC-5 caused VIT-2 aggregation in enlarged vacuoles (Fig. 8, A and A′), similar to the effects of depleting RME-1, implying a shared functional step between exocyst and RME-1. Next, we analyzed VIT-2 localization in animals lacking both SEC-5 and RAB-10 or EHBP-1. The intestinal distribution of VIT-2 resembles that of *rab-10* or *ehbp-1* mutants, with fewer vacuoles being observed (Fig. 8, B and B′). Given the lack of interaction between RAB-10 and the exocyst (Chen et al., 2014), our evidence suggests that the exocyst acts downstream of RAB-10-EHBP-1, likely positioned between recycling endosomes and the plasma membrane (Pereira et al., 2023; Mei and Guo, 2018). It is worth noting that *sec-5(tm1443)*, *sec-10(txu1)*, and *sec-15(RNAi)* animals have recycling defects (Chen et al., 2014). However, the knockdown of SEC-10 and SEC-15 had a minimal effect on VIT-2 secretion, suggesting that the exocyst subunits possess functionalities distinct from those of the complex.

Recent studies indicate that the FERARI complex serves as a tether for sorting endosomes in *C. elegans* and mammals, contributing to endocytic recycling (Solinger et al., 2020, 2022). Nevertheless, the loss of FERARI elements (RABS-5, VPS-45, SPE-39, and RFIP-2) did not significantly affect the distribution of VIT-2 across tissues (Fig. S3, C and C′). These data are consistent with the proposition that FERARI is specifically engaged in facilitating apical recycling (Solinger et al., 2020, 2022).

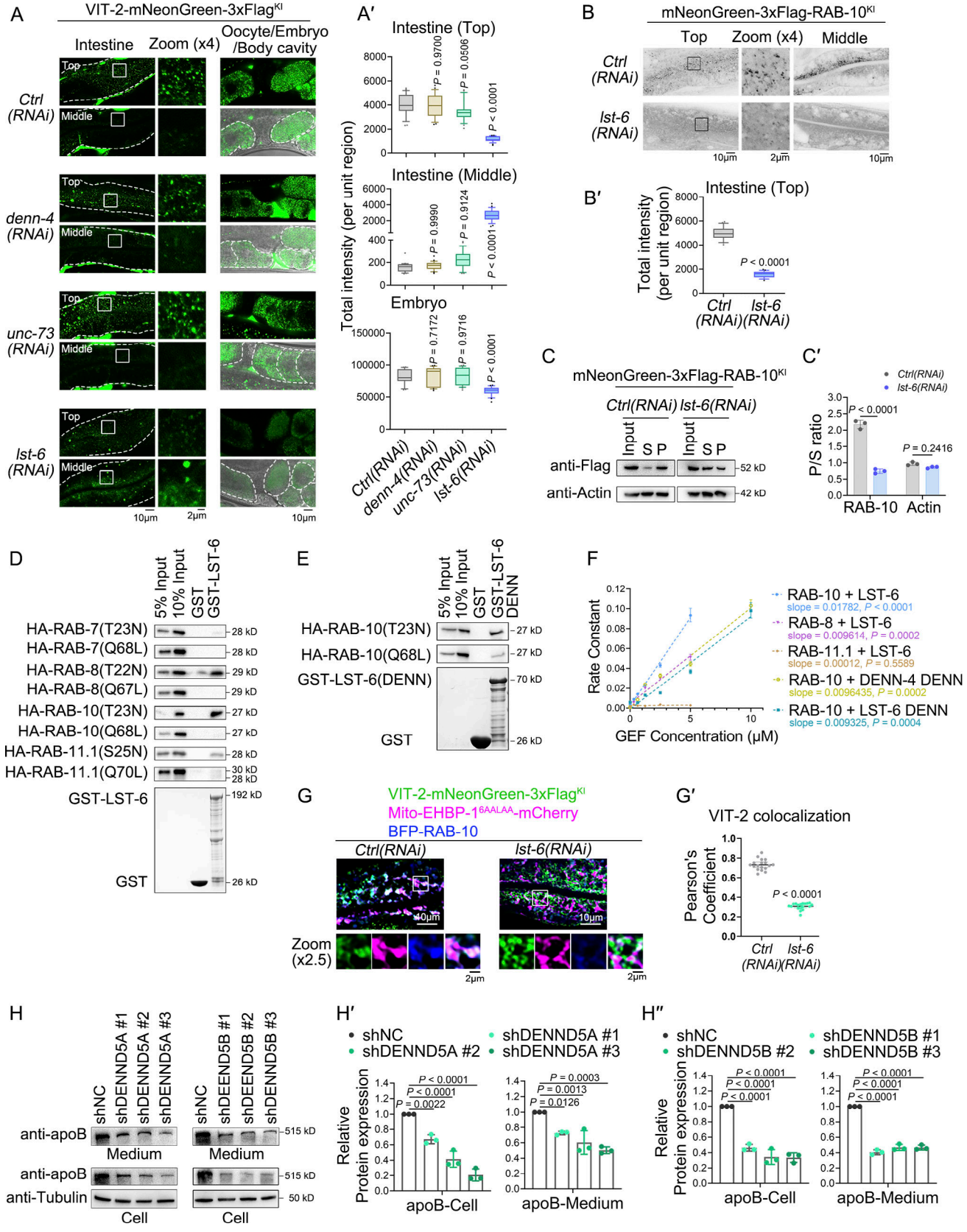

Figure 7. **LST-6/DENND5 acts as a GEF for RAB-10. (A and A′)** Confocal images showing the distribution of VIT-2-mNeonGreen-3xFlag^{KI} in the *C. elegans* intestine, oocytes, and embryos in different gene knockdown backgrounds. **(B and B′)** Confocal images showing the subcellular localization of mNeonGreen-3xFlag-RAB-10^{KI}. The statistical data are shown as box-and-whisker plots with 10th–90th percentile (n = 24 cells from eight animals of each genotype; dots, outliers; boundaries, quartiles; one-way ANOVA test with Dunn's multiple comparison in A′; two-tailed Mann-Whitney test in B′). **(C and C′)** Western blot

analysis of the membrane-to-cytosol ratio of RAB-10 in control or *lst-6(RNAi)* animals. Band intensity was quantified by using the "Plot Lanes" function in Image J; error bars are 95% CIs (two-tailed Student's *t* test) (*n* = 3 independent experiments). S: supernatant; P: pellet. **(D and E)** Western blotting showing GST pull-down detected protein interactions. **(F)** The rate constant of GTP exchange was analyzed using nonlinear regression (Exponential-One phase decay, Y0 = 100, Plateau = 50). A scatter diagram with protein concentration as the x-axis and GEF rate constant as the y-axis was generated and analyzed using linear regression. The slope and the slope significantly non-zero P value were shown. **(G and G′)** Confocal images showing colocalization between VIT-2-mNeonGreen-3xFlag^{KI} and mitochondria. The statistical analysis of colocalization was calculated as Pearson's correlation coefficient and shown as mean ± SD (*n* = 18 cells from six animals of each genotype; two-tailed Mann–Whitney test). **(H–H″)** Western blot analysis of apoB protein levels in Huh7 cells. Band intensity was measured using the "Plot Lanes" function in ImageJ from three independent experiments. Error bars represent 95% CIs (one-way ANOVA test with Dunn's multiple comparison). Source data are available for this figure: SourceData F7.

Discussion

The Caplan group has demonstrated the importance of EHBP1 in linking Rab10-associated vesicles to KIF13 motor proteins, influencing vesicle positioning and possible clustering (Farmer et al., 2021). Our study reveals a distinct mechanism involving RAB-10 and EHBP-1 that facilitates the convergence of exocytic vesicular carriers. Notably, we identified LST-6/DENND5 as a specific GEF for RAB-10 in this pathway, underscoring the

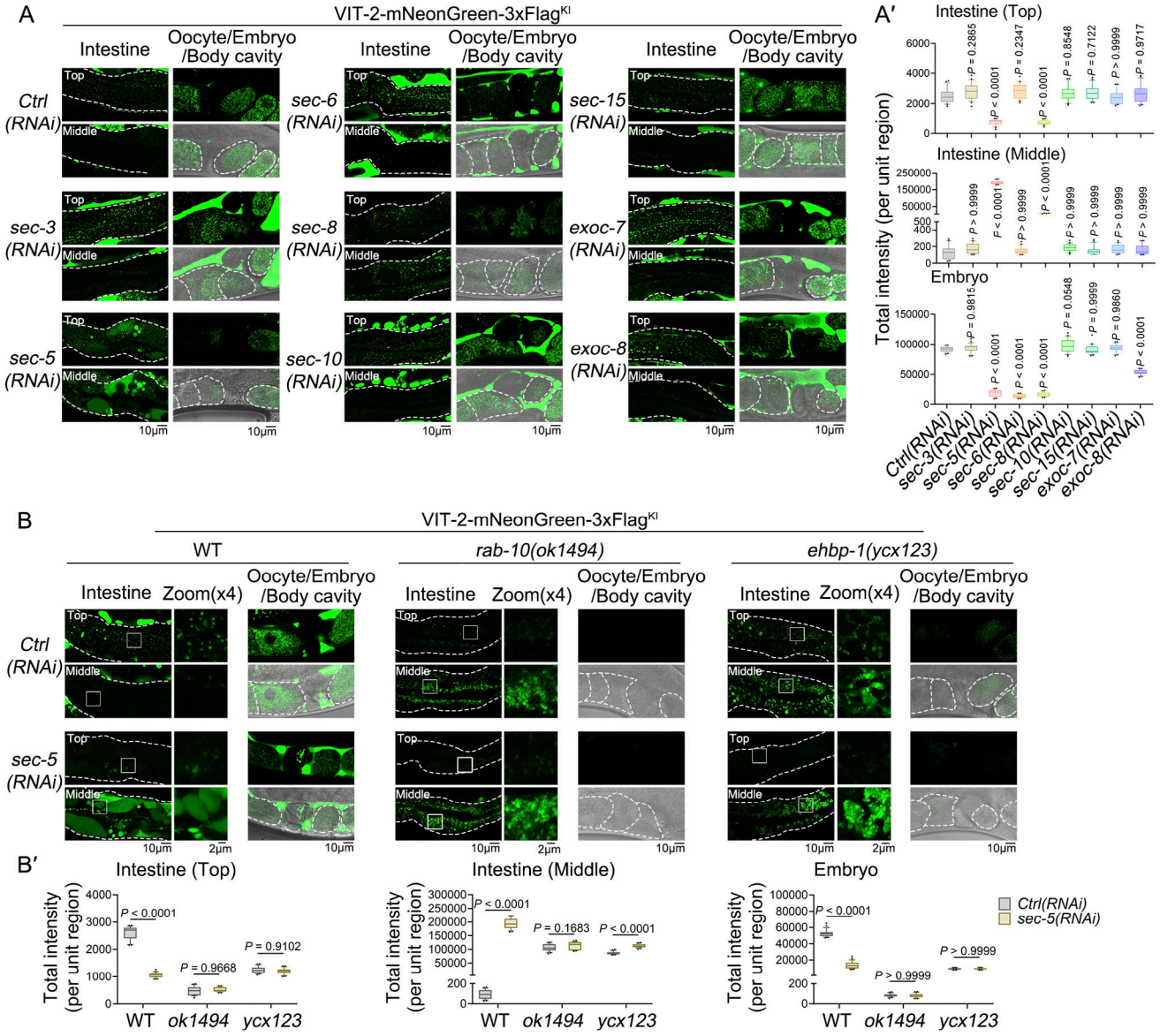

Figure 8. **The exocyst complex functions downstream of RAB-10-EHBP-1 in secretion. (A–B′)** Confocal images showing the distribution of VIT-2-mNeonGreen-3xFlag^{KI} in the *C. elegans* intestine, oocytes, and embryos in different gene knockdown backgrounds. Statistical data is shown as box-and-whisker plots with 10th–90th percentile (*n* = 24 cells from eight animals of each genotype; dots, outliers; boundaries, quartiles; one-way ANOVA test with Dunn's multiple comparison used in A′, two-way ANOVA with Bonferroni post-test used in B′).

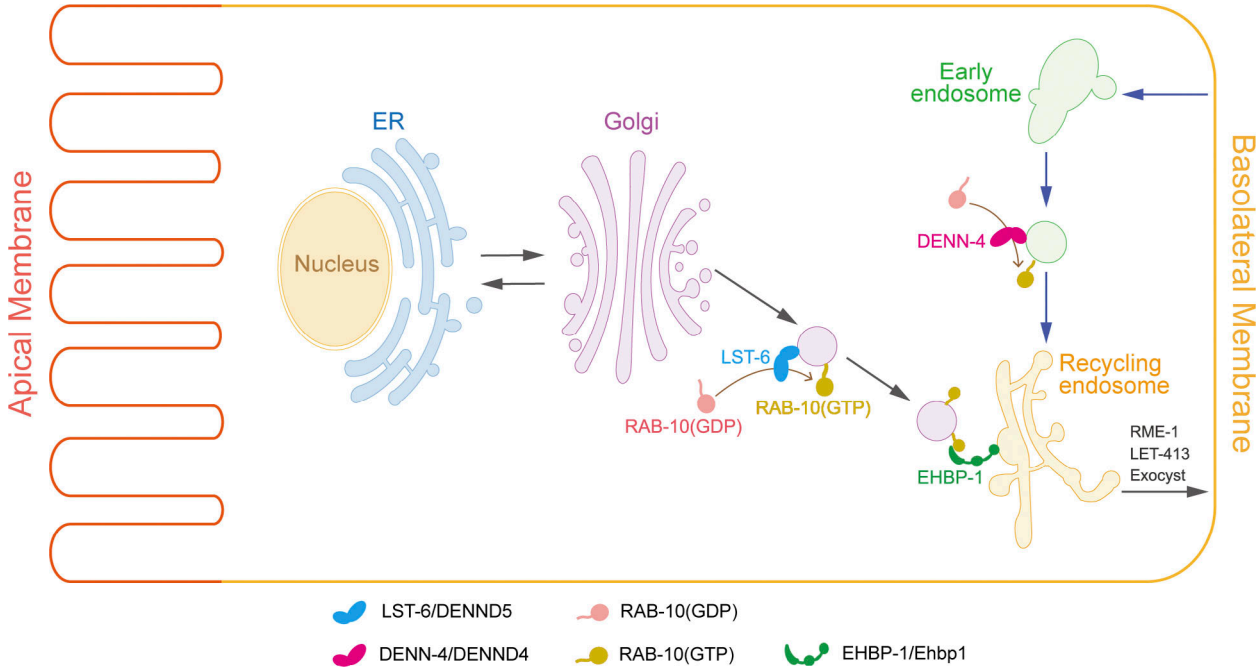

Figure 9. **The role of EHBP-1, RAB-10, and LST-6 in facilitating post-Golgi exocytic trafficking.** LST-6 acts as a GEF to enhance the functionality of RAB-10 during basolateral exocytosis, a role distinct from DENN-4, which serves as a GEF in basolateral recycling. EHBP-1, situated on recycling endosomes, captures RAB-10-positive post-Golgi exocytic carriers, facilitating the delivery of exocytic cargos to recycling endosomes. Ultimately, these cargos are transported to the plasma membrane, a process likely reliant on the functions of RME-1, LET-413, and the exocyst complex.

intricate and specialized nature of trafficking mechanisms and suggesting that distinct GEFs may activate RAB-10 for different trafficking routes (Fig. 9).

Our study found a reduction in apoB levels after Rab10 knockdown. Moreover, the levels of the secretory membrane protein SLCF-1 decreased in *rab-10* and *ehbp-1* mutants. These observations point to a redirection of secretory cargo to lysosomes in the absence of RAB-10 or EHBP-1. Indeed, accumulation of VIT-2 occurred in the intestinal cells of *rab-10* and *ehbp-1* mutants, exhibiting colocalization with the lysosome marker. It is noteworthy that the accumulation of VIT-2 is more significant in *rab-10* mutants compared with *ehbp-1* mutants; however, no difference in the severity of secretion defects was observed when using SLCF-1 as the cargo. Our results indicate that EHBP-1 localizes to recycling endosomes, where it captures exocytic vesicles labeled with RAB-10. Hence, it is conceivable that RAB-10 functions upstream of EHBP-1. The absence of the upstream molecular switch RAB-10 is likely to have a more pronounced effect on the transport, while downstream, apart from EHBP-1, there may exist other unidentified regulators capable of providing compensatory functions. In addition, the absence of the EHBP-1 results in embryonic lethality, hindering progression to the adult stage. Thus, we used a heat shock–inducible *ehbp-1* conditional mutant to minimize developmental impact, potentially resulting in less severe VIT-2 phenotypes compared with *rab-10* mutants. The similarity in SLCF-1 phenotype between *ehbp-1* and *rab-10* mutants could be attributed to the levels of SLCF-1. Distinguishing the phenotype of transgenic SLCF-1-GFP in *ehbp-1* conditional mutants from that of *rab-10* mutants is complicated by the low expression of SLCF-1-GFP, which hinders effective capture of the residual SLCF-1 signal in *ehbp-1* mutants.

The presence of subdomains on the recycling endosome has been well-documented. In MDCK cells, the apical and basolateral proteins are segregated into subdomains within recycling endosomes (Thompson et al., 2007). In a recent study, the dynamics of recycling endosome maturation were traced, revealing distinct subdomains that were marked with Rab11 (Podinovskaia et al., 2021). Our results further suggest that basolateral recycling endosomes operate via distinct subdomains, namely exocytic and recycling domains. These findings raise inquiries regarding the mechanisms governing compartmentalization within the recycling endosome. In addition to lipid composition modulation, proteins are pivotal in establishing and maintaining endosomal subdomains. Recent research has highlighted the Rab3 family's essential role in localizing microdomain-associated proteins to the plasma membrane (Diaz-Rohrer et al., 2023). In addition, protein complexes could act as molecular barriers, segregating different components within designated regions of the organelle (Edidin, 1992). To gain a deeper understanding of the formation, maintenance, and dynamic restructuring of subdomains within recycling endosomes, the utilization of super-resolution real-time imaging techniques is imperative.

GEFs are responsible for activating Rabs on diverse membrane compartments (Hutagalung and Novick, 2011), with their specific localization exerting a substantial impact on Rabs distribution (Blumer et al., 2013). UNC-73/TRIO and DENN-4/DENND4 are reported to act as GEFs implicated in regulating RAB-10 activation (Tao et al., 2019; Liu et al., 2018). While UNC-73/TRIO features a RhoGEF domain, DENN-4/DENND4 is characterized by the

presence of a DENN domain. DENND5, which also harbors a DENN domain, was initially characterized as a Rab6-binding protein (R6IP1) in mice (Janoueix-Lerosey et al., 1995). Subsequently, its presence was confirmed in various species, such as humans, chickens, cows, and zebrafish. Examination of tissue expression patterns in mice demonstrated that the brain exhibits a higher prevalence of the splice variant R6IP1A, while the intestine predominantly expresses R6IP1B (Miserey-Lenkei et al., 2007). Of note, R6IP1 has been shown to associate Golgi-localized Rab6 with recycling endosome-associated Rab11A during metaphase and cytokinesis (Miserey-Lenkei et al., 2007). To assess the potential coupling efficiency of LST-6 with RAB-6 and RAB-10, we conducted preliminary tests. Nevertheless, the loss of the Rab6 homologs RAB-6.1/RAB-6.2 did not affect the localization of VIT-2 in intestinal cells and oocytes (Fig. S5. O and O′). Also, the punctate pattern of RAB-10 in intestinal cells remained unchanged (Fig. S5, P and P′). These results suggest that there is no apparent impact of RAB-6 on the functionality of RAB-10 via LST-6 in the basolateral exocytosis. In addition, it has been reported that DENND5 functions as a Rab39 GEF (Yoshimura et al., 2010). The expression of *C. elegans* RAB-39 is limited to the pharynx, neurons, and vulva (Takenaka et al., 2013). Indeed, the loss of RAB-39 did not lead to apparent defects in the intestinal secretion of VIT-2 (Fig. S1 and Fig. S2 A). Thus, we opted not to explore the role of RAB-39 in basolateral exocytosis further.

It has been noted in prior research that R6IP1 interacts with Rab6 independently of nucleotide specificity, whereas its association with Rab11A is reliant on GTP binding (Miserey-Lenkei et al., 2007). However, our observation notes that LST-6 binds to inactive RAB-11.1. Potential explanations for this discrepancy include species-specific differences and variations in experimental conditions. Species-specific differences may arise from divergent protein behaviors between mammals and *C. elegans*, potentially influenced by evolutionary changes in protein binding preferences. Future research should include direct comparative studies of R6IP1 and LST-6 binding to their respective Rab proteins under consistent experimental conditions.

Materials and methods

General methods and strains

All *C. elegans* strains were derived from the Bristol N2 strain and cultured using standard protocols, involving growth on nematode growth medium plates at 20°C and feeding with the OP50 strain of *E. coli*. The specific strains utilized in this investigation are detailed in Table S1. In this study, three types of fluorescent protein–labeled strains were utilized. The first involved inserting the fluorescent tag coding sequence into the gene to label endogenous proteins, denoted as "KI" (knock-in) in the nomenclature. If the endogenous expression levels were insufficient for imaging, the second approach was employed, wherein a single copy was inserted into the genome using CRISPR-Cas9 technology under the control of the intestine-specific promoter Pvha-6, labeled as "SC" (single-copy). The third type consisted of extra-chromosome transgene arrays with higher copy numbers, without any additional labeling in the nomenclature.

RNA interference

RNA interference (RNAi) was induced in *C. elegans* through ingestion of *E. coli* HT115 strain containing the L4440 vector that expresses specific double-stranded RNA (dsRNA) targeting the gene of interest (Rual et al., 2004; Kamath and Ahringer, 2003). Typically, young adult hermaphrodites were nourished with HT115 and the F1 offspring were subsequently analyzed. To prevent severe illness due to gene knockdown, RNAi feeding was performed on *snap-29*, *snap-1*, *sec-5*, *sec-8*, *rab-1*, *rab-5*, *syx-18*, *ykt-6*, *apm-1*, and *aps-1* during the L2–L3 stage of the nematode, followed by evaluation in the same generation at the young adult stage. The efficiency of RNAi was assessed through real-time PCR analysis and is summarized in Table S2.

Antibodies

The antibodies used in this study include a mouse anti-Flag monoclonal antibody (F1804; Sigma-Aldrich), a rabbit anti-HA monoclonal antibody (C29F4; Cell Signaling Technology), a mouse anti-GFP monoclonal antibody (AG281; Beyotime), a mouse anti-α-tubulin monoclonal antibody (T6199; Sigma-Aldrich), a mouse anti-actin monoclonal antibody (sc-47778; Santa Cruz Biotechnology), a rabbit anti-mCherry polyclonal antibody (ab167453; Abcam), a rabbit anti-Rab10 monoclonal antibody (#8127; Cell Signaling), and a goat anti-Apolipoprotein B polyclonal antibody (600-101-111; Rockland).

Transgenic strains

The *vha-6* promoter governs the expression of genes specific to the intestine. Initially, cDNA was integrated into pDONR221 using the BP reaction and then transferred into a destination vector containing a Gateway cassette through the LR reaction. A standard microinjection technique was employed to produce the transgenic strains.

CRISPR/Cas9 mutant strains

The pOG2034 vector, originally containing the *eft-3* promoter in pDD162 (#47549; Addgene), was modified by replacing the *eft-3* promoter with the heat-shock promoter *Phsp-16.2*. This modification enables inducible CRISPR/Cas9-mediated gene knockdown upon heat shock treatment. The crRNA sequences were designed using an online CRISPR guide RNA selection tool (http://genome.sfu.ca/crispr/search.html). Three sequences (5′-GAACACTCTTGTACATCGAC-3′, 5′-GTCTTATTCTCATCAGAACG-3′, and 5′-TCAAAAGTTATTTGCAACTG-3′) targeting the C-terminus of EHBP-1 were chosen and inserted into the pOG2034 vector, respectively. The plasmids were introduced into DH5α competent cells, and subsequent sequencing of bacterial clones was carried out to confirm the fidelity of the target sequences. Transgenic animal *ycx123* was ultimately produced through the microinjection of these three plasmids (at a concentration of 50 ng/μl) and a selection marker *Podr-1::gfp* into the germline of N2 hermaphrodites.

CRISPR/Cas9 knock-in strains

Two crRNAs were designed as described and inserted into pDD162 individually to achieve highly efficient cutting of the target sequence. For homology recombination-mediated knock-in, 500-bp

homologous arms flanking the cutting site were cloned into the pUC19 vector. The construct featured a coding sequence for mNeonGreen and a Self-Excising Drug Selection Cassette (SEC) located between the two homologous arms (Dickinson et al., 2015). Subsequently, three plasmids were microinjected into the worm germline, with pDD162 at a concentration of 5 ng/µl and the pUC19 vector at 25 ng/µl. Knock-in progenies can be effectively screened using roller and hygromycin resistance phenotypes, and the SEC sequence can be eliminated through heat shock. The knock-in strains were confirmed through genotyping and sequencing. The crRNA sequences for *vit-2* are 5′-ACCGCCTGCGTCGCTTATTG-3′ and 5′-CTCTTTCGTTGAGTCTGTCA-3′, and for *rab-10* they are 5′-TGAAGAGCATGTCATACGGT-3′ and 5′-AATTTGAAGAGCATGTCATA-3′. Single-copy strains were also constructed using CRISPR-Cas9. The ttTi4348 and ttTi5605 genome loci were used as insertion sites on chromosomes I and II, respectively (Xu et al., 2016).

C. elegans western blotting and coimmunoprecipitation

In the case of the VIT-2-mNeonGreen-3xFlag strain, synchronized worms were cultured until reaching the young adult stage and subsequently subjected to bleaching for egg collection. The addition of 5 vol of RIPA lysis buffer (Beyotime) was followed by ultrasonication and centrifugation to eliminate debris. To prevent degradation, the samples were kept on ice. A protein loading buffer was then added to the samples, which were subsequently boiled at 100°C for 10 min. This was succeeded by SDS-PAGE and immunoblot analysis to assess the expression level of the VIT-2 protein. For coimmunoprecipitation (co-IP) studies, worms were collected and subjected to lysis using RIPA buffer. Homogenization was performed using an automatic tissue grinder (JX-FSTPRP; Jingxin Inc.). The subsequent steps involved processing the samples for the analysis of the target protein bands.

Quantitative PCR (qPCR)

Synchronized worms were collected and washed with M9 buffer, while HepG2 cells were collected and washed using PBS. Total RNA was extracted using the RNeasy Plus Mini Kit (Qiagen), and cDNA synthesis was performed with the RevertAid First Strand cDNA Synthesis Kit (Thermo Fisher Scientific). Real-time PCR was conducted using iTaq Universal SYBR Green Supermix (Bio-Rad) and monitored with the CFX Connect Real-Time PCR Detection System (Bio-Rad).

GST pull-down assay

Utilizing Gateway BP and LR reactions, cDNAs were integrated into pGEX-2T or pcDNA3.1-2xHA vectors harboring a Gateway cassette. HA-tagged proteins were generated in vitro using the TNT Coupled Transcription/Translation System (Promega) with pcDNA3.1 vectors as templates. The expression of GST-fused proteins was achieved by introducing pGEX-2T vectors into Rosetta2 (DE3) competent cells (Novagen) and inducing them with IPTG. The bacteria were collected and lysed at 4°C in a bacterial lysis buffer (50 mM Tris pH 8.0, 300 mM NaCl, 2 mM DTT, 1 mM PMSF, 1% [vol/vol] NP-40, and a protease inhibitor) using a high-pressure cracker. The protein lysate was incubated with 30 µl of glutathione sepharose 4B beads (GE Healthcare) at 4°C for 4 h, followed by five washes with wash buffer (50 mM Tris pH 8.0, 300 mM NaCl, 2 mM DTT, and 0.2% NP-40) at 4°C. Subsequently, the beads were exposed to TNT products overnight. Unbound proteins were removed through additional washes, and the samples were subjected to SDS-PAGE and western blotting analysis.

Protein expression and purification

The codon-optimized cDNA sequences of *ehbp-1(ΔC2)* and *ehbp-1(ΔC2 ΔCC)* were inserted into the pGEX-6p vector. The cDNA sequences of *rab-10(CC199SS)*, *rab-8*, and *rab-11.1* were inserted into the pPICZ vector (Invitrogen). The *rab-10(CC199SS)*, *rab-8*, and *rab-11.1* construct contained a C-terminal 6×His tag, while *ehbp-1(ΔC2)* and *ehbp-1(ΔC2 ΔCC)* were equipped with a N-terminal StrepII tag and GST tag. Subsequently, the fusion proteins of RAB-10(CC199SS), RAB-8, and RAB-11.1 were produced in Pichia pastoris (X-33) Competent Cells (Invitrogen). Pichia pastoris cells expressing the 6×His-tagged protein were cultured in a shaker at 30°C. The cells were pelleted and lysed using a high-pressure homogenizer on ice in yeast lysis buffer (50 mM HEPES pH 8.0, 150 mM NaCl, 1 mM PMSF, and 1% [vol/vol] NP-40). To purify the 6×His-tagged protein, the protein supernatant was incubated with Ni-NTA resin (Qiagen) in yeast lysis buffer supplemented with 30 mM imidazole at 4°C for 4 h. Subsequently, the beads were washed five times with a washing buffer composed of 50 mM Tris (pH 8.0), 150 mM NaCl, 30 mM imidazole, and 0.2% (vol/vol) NP-40. Following this, the beads were exposed to the hydrolysis-resistant GTP analog GMP-PNP or GDP (Merck) at a final concentration of 0.1 mM. The proteins were eluted with 500 mM imidazole in a solution containing 50 mM Tris (pH 8.0) and 150 mM NaCl. For the purification of GST and StrepII-tagged proteins, the bacteria were collected and lysed at 4°C in a bacterial lysis buffer (50 mM HEPES [pH 8.0], 150 mM NaCl, 2 mM DTT, 1 mM PMSF, 1% [vol/vol] NP-40, and a protease inhibitor) using a high-pressure homogenizer on ice. The protein lysate was incubated with 1 ml of glutathione sepharose 4B beads (GE Healthcare) at 4°C for 4 h, followed by five washes with wash buffer (50 mM Tris pH 8.0, 300 mM NaCl, 2 mM DTT, and 0.2% NP-40) at 4°C. The proteins were cleavaged by PreScission Protease in PreScission cleavage buffer (50 mM Tris [pH 8.0], 150 mM NaCl, 2 mM DTT, and 1 mM EDTA) at 4°C overnight.

Liposome tethering assay

The lipids utilized in liposome preparation include 16:0–18:1 PC, DOPS, DOGS-NiNTA (Avanti), and DiO (Thermo Fisher Scientific). These lipids were dissolved in chloroform and stored at −30°C. For tethering assays, the liposome compositions were formulated with a ratio of PC:DOPS:DOGS-NiNTA:DiO at 80:15:3:2. The solvent was evaporated under nitrogen and vacuumed for 4 h, followed by suspension of the lipids in liposome buffer (20 mM HEPES, 100 mM KCl, pH 8.0). The mixture was rapidly vortexed, subjected to five freeze–thawing cycles by immersion in liquid nitrogen and a 55°C water bath, and extruded through two polycarbonate membranes with a pore diameter of 100 nm (Avestin) for 39 passes. The liposomes were then stored at 4°C and utilized within 2 days for the liposome tether assay. The

coverslip and slide underwent sonication with water and acetone, followed by PEG-Biotin coating. Flow chambers were constructed using coverslips and slides secured with double-sided tape. Experiments were carried out in a liposome buffer containing 5 mM $MgCl_2$. Initially, NeutrAvidin at 0.2 mg/ml was introduced into the chambers, washed, and then 18 µM StrepII-EHBP-1 (ΔC2) or StrepII-EHBP-1 (ΔC2 ΔCC) was injected at varying concentrations to immobilize proteins on the coverslip. Subsequently, liposomes (containing PC, DOPS, DOGS-Ni-NTA, and Dio) and RAB-10(CC199SS)-6×His loaded with GDP or GMP-PNP at 100 nM were mixed in low-binding tubes, incubated for 15 min, washed, and promptly imaged to observe liposome capture. Fluorescence signals were captured using a Nikon TIRF microscope equipped with a 100× (NA 1.45) oil objective.

Confocal microscopy and image analysis

Live worms were placed on a 2% agar plate containing a drop of 20 mM levamisole and were observed using a Nikon C2 confocal microscope equipped with a 100× oil objective (numerical aperture 1.4). Z-stack optical sections were captured at 1.0-µm intervals with excitation wavelengths of 405, 488, or 594 nm and captured using NIS-Elements AR 4.40.00 software at room temperature. Tracking the dynamics of vesicles was achieved using a spinning disk confocal microscope (ANDOR Dragonfly/CR-DFLY-201-40) equipped with a 63× objective (numerical aperture 1.4) using Fusion 2.3.0.36 software at room temperature. Fluorescence intensities and area analyses were conducted on 24 cells from eight animals per genotype using Metamorph software (version 7.10.3.279). Colocalization analysis involved the observation of 18 cells from six animals, with Pearson's correlation coefficient calculated using the JACoP plugin in Fiji (ImageJ) software.

Cell culture, transfection, and immunofluorescence assay

HEK293T, HepG2, and Huh7 cells were cultured in Dulbecco's Modified Eagle Medium (DMEM) supplemented with 10% fetal bovine serum (FBS) (Gibco) and 2 mM glutamine (Gibco) at 37°C. Transfection of HEK293T cells utilized lipofectamine 2000, while HepG2 cells were transfected using lipofectamine 3000 (Thermo Fisher Scientific). Short hairpin RNAs (shRNAs) targeting Rab10 or EHBP1 were cloned into the pLKO.1 vector. The sequences of the shRNAs used were as follows: shNC (negative control), 5′-CCTAAGGTTAAGTCGCCCTCGC-3′; shRab10 #1, 5′-AATGAAGATGTGGAAAGAATG-3′; shRab10 #2, 5′-AAGGAAAGAAGATCAAGCTAC-3′; shDENND5a #1, 5′-ATCTAACTGGCTATGTTATTA-3′; shDENND5a #2, 5′-CCCAATTCCATGCCTTTATTA-3′; shDENND5a #3, 5′-TACAGTATGGCCCACTTAATA-3′; shDENND5b #1, 5′-GCCCACTATCCTCAGAATATA-3′; shDENND5b #2, 5′-CCAGGGAGGTCACTGAAATTT-3′; shDENND5b #3, 5′-CAGATGTTTGCCACCTTTATT-3′. The pLKO.1 vectors were co-transfected with lentivirus packaging plasmids psPAX2 and pMD.2G at a ratio of 2:1:1 in HEK293T cells. Subsequently, cell culture media containing shRNA-expressing Lentiviruses was collected and filtered. Following this, HepG2 cells were infected with different lentiviruses and screened for stable knockdown cell lines using 0.4 µg/ml puromycin. Before immunofluorescence staining, cells were cultured on a confocal dish for 24 h. After fixation with 4% paraformaldehyde, the cells were blocked with a PBS solution containing 5% FBS and 0.3% Triton X-100 for 1 h. Then, the cells were incubated with primary and secondary antibodies, and images were captured using a Nikon TIRF microscope.

In vitro GEF assay

The GEF assay was conducted as follows (Kanie and Jackson, 2018): Purified RAB-10(CC199SS)-6×His, RAB-8-6×His, and RAB-11.1-6×His at a concentration of 150 µM were incubated with 1.5 mM MANT-GDP in a loading buffer (20 mM HEPES [pH 8.0], 50 mM NaCl, 0.25 M EDTA, and 100 mM DTT) for 90 min. Subsequently, 10 mM $MgCl_2$ was added to halt the reaction for 30 min. To eliminate unbound MANT-GDP, the MANT-GDP-loaded RAB-10(CC199SS)-6×His, RAB-8-6×His, and RAB-11.1-6×His were passed through a NAP-5 gel filtration column (Cytiva) and washed with nucleotide exchange buffer (40 mM HEPES [pH 8.0], 50 mM NaCl, 10 mM $MgCl_2$, and 2 mM DTT). Next, 50 µM of preloaded His-tagged proteins were incubated at 25°C with GST-tagged proteins and the hydrolysis-resistant GTP analog GMP-PNP (100 mM) in the nucleotide exchange buffer. The nucleotide exchange reaction was monitored using a Synergy 2 MultiMode Reader (BioTek) with excitation at 360 nm and emission at 440 nm.

Membrane fractionation assay

Synchronization and collection of animals at the young adult stage was carried out using M9 buffer, followed by resuspension in 5 vol of lysis buffer (50 mM Tris [pH 8.0], 20% sucrose, 10% glycerol, 1 mM DTT, and a protease inhibitor cocktail). The worms were lysed and centrifuged at 10,000 *g* for 10 min at 4°C. A 40-µl aliquot of the cleared lysate was then centrifuged at 100,000 *g* for 1 h. The resulting supernatant was collected, and the pellet was resuspended in the lysis buffer. Both the supernatant and pellet underwent analysis via western blotting.

Electron microscopy

The young adult intestine, exposed by cutting with needles, and synchronized eggs were initially fixed using 2.5% glutaraldehyde, followed by fixation with 1% OsO_4 in 0.1 M phosphate buffer (pH 7.4) for 2 h at room temperature. Subsequently, they were rinsed three times in 0.1 M phosphate buffer (pH 7.4), each time for 15 min. The sample was dehydrated, infiltrated with resin, and embedded in epoxy resin. Following this, the sample was sectioned into 80- to 100-nm slices, stained with uranium acetate and lead, and examined using a Talos L120C transmission electron microscope at an accelerating voltage of 120 kV.

Statistical analysis

Statistical analyses were conducted using GraphPad Prism 8.02 software (GraphPad Software). Data distribution was assumed to be normal, but this was not formally tested. Biochemical datasets were assessed using a *t* test. Imaging datasets were analyzed through a one-way ANOVA, followed by Dunn's post hoc multiple comparison test for datasets with more than two variables. Alternatively, a Mann–Whitney *U* test was used for datasets with only two variables. When dealing with grouped datasets, a two-way ANOVA test was employed.

Online supplemental material

Fig. S1 presents representative image data from an RNAi screening of yolk exocytosis regulation involving 22 Rabs. Fig. S2 indicates that RAB-10 and EHBP-1 are not involved in apical exocytosis, and their absence is likely to result in the lysosomal degradation of basolateral exocytic cargos. Fig. S3 displays data from RNAi screens targeting yolk exocytosis regulators, specifically examining recycling regulators, RAB-10 effectors, and FERARIs. Fig. S4 presents the data supporting that EHBP-1 sequesters exocytic carriers by a mechanism reliant on RAB-10. Fig. S5 demonstrates the role of LST-6/DENND5 as a GEF for RAB-10, aiding in exocytic transport. Table S1 provides a list of the *C. elegans* strains utilized in the study. Table S2 presents the qPCR primers and corresponding results. Videos 1 and 2 depict the dynamics of RAB-10-labeled endosomes corresponding to Fig. 3 F.

Data availability

All data supporting the findings of this study are present in the paper and its supplemental materials. In addition, the source data is available with the paper.

Acknowledgments

This work was supported by the National Key R&D Program of China (2021YFA1300302) to A. Shi, the National Natural Science Foundation of China (92354305) to Y. Yan, the National Natural Science Foundation of China (92357302, 32320103007, 32130027) to A. Shi, and the National Natural Science Foundation of China (32400568) to J. Zhang. The funders had no role in study design, data collection and analysis, decision to publish, or preparation of the manuscript.

Author contributions: S. Liu: Conceptualization, Data curation, Formal analysis, Investigation, Methodology, Project administration, Resources, Software, Supervision, Validation, Visualization, Writing - original draft, Writing - review & editing, J. Wei: Conceptualization, Data curation, Formal analysis, Investigation, Methodology, Project administration, Resources, Software, Supervision, Validation, Visualization, Writing - original draft, Writing - review & editing, L. Zhong: Data curation, Investigation, S. Hai: Data curation, Investigation, S. Song: Data curation, Investigation, C. Xie: Data curation, Investigation, Z. Huang: Data curation, Investigation, Z. Cheng: Methodology, J. Zhang: Resources, A. Du: Investigation, Resources, Software, P. Zhang: Investigation, Resources, Software, Y. Yan: Conceptualization, Data curation, Formal analysis, Funding acquisition, Investigation, Methodology, Project administration, Resources, Software, Supervision, Validation, Visualization, Writing - original draft, Writing - review & editing, A. Shi: Conceptualization, Data curation, Formal analysis, Funding acquisition, Investigation, Methodology, Project administration, Resources, Software, Supervision, Validation, Visualization, Writing - original draft, Writing - review & editing.

Disclosures: The authors declare no competing interests exist.

Submitted: 1 October 2024
Revised: 5 January 2025
Accepted: 22 January 2025

References

Ang, A.L., H. Fölsch, U.M. Koivisto, M. Pypaert, and I. Mellman. 2003. The Rab8 GTPase selectively regulates AP-1B-dependent basolateral transport in polarized Madin-Darby canine kidney cells. *J. Cell Biol.* 163: 339–350. https://doi.org/10.1083/jcb.200307046

Ang, A.L., T. Taguchi, S. Francis, H. Fölsch, L.J. Murrells, M. Pypaert, G. Warren, and I. Mellman. 2004. Recycling endosomes can serve as intermediates during transport from the Golgi to the plasma membrane of MDCK cells. *J. Cell Biol.* 167:531–543. https://doi.org/10.1083/jcb.200408165

Babbey, C.M., N. Ahktar, E. Wang, C.C. Chen, B.D. Grant, and K.W. Dunn. 2006. Rab10 regulates membrane transport through early endosomes of polarized Madin-Darby canine kidney cells. *Mol. Biol. Cell.* 17:3156–3175. https://doi.org/10.1091/mbc.e05-08-0799

Babbey, C.M., R.L. Bacallao, and K.W. Dunn. 2010. Rab10 associates with primary cilia and the exocyst complex in renal epithelial cells. *Am. J. Physiol. Renal Physiol.* 299:F495–F506. https://doi.org/10.1152/ajprenal.00198.2010

Balklava, Z., S. Pant, H. Fares, and B.D. Grant. 2007. Genome-wide analysis identifies a general requirement for polarity proteins in endocytic traffic. *Nat. Cell Biol.* 9:1066–1073. https://doi.org/10.1038/ncb1627

Blümer, J., J. Rey, L. Dehmelt, T. Mazel, Y.W. Wu, P. Bastiaens, R.S. Goody, and A. Itzen. 2013. RabGEFs are a major determinant for specific Rab membrane targeting. *J. Cell Biol.* 200:287–300. https://doi.org/10.1083/jcb.201209113

Bonifacino, J.S., and B.S. Glick. 2004. The mechanisms of vesicle budding and fusion. *Cell.* 116:153–166. https://doi.org/10.1016/S0092-8674(03)01079-1

Brunet, S., and M. Sacher. 2014. Are all multisubunit tethering complexes bona fide tethers? *Traffic.* 15:1282–1287. https://doi.org/10.1111/tra.12200

Casanova, J.E., X. Wang, R. Kumar, S.G. Bhartur, J. Navarre, J.E. Woodrum, Y. Altschuler, G.S. Ray, and J.R. Goldenring. 1999. Association of Rab25 and Rab11a with the apical recycling system of polarized Madin-Darby canine kidney cells. *Mol. Biol. Cell.* 10:47–61. https://doi.org/10.1091/mbc.10.1.47

Chen, C.C., P.J. Schweinsberg, S. Vashist, D.P. Mareiniss, E.J. Lambie, and B.D. Grant. 2006. RAB-10 is required for endocytic recycling in the Caenorhabditis elegans intestine. *Mol. Biol. Cell.* 17:1286–1297. https://doi.org/10.1091/mbc.e05-08-0787

Chen, D., C. Yang, S. Liu, W. Hang, X. Wang, J. Chen, and A. Shi. 2018. SAC-1 ensures epithelial endocytic recycling by restricting ARF-6 activity. *J. Cell Biol.* 217:2121–2139. https://doi.org/10.1083/jcb.201711065

Chen, S., L. Li, J. Li, B. Liu, X. Zhu, L. Zheng, R. Zhang, and T. Xu. 2014. SEC-10 and RAB-10 coordinate basolateral recycling of clathrin-independent cargo through endosomal tubules in Caenorhabditis elegans. *Proc. Natl. Acad. Sci. USA.* 111:15432–15437. https://doi.org/10.1073/pnas.1408327111

Chen, W., Y. Feng, D. Chen, and A. Wandinger-Ness. 1998. Rab11 is required for trans-golgi network-to-plasma membrane transport and a preferential target for GDP dissociation inhibitor. *Mol. Biol. Cell.* 9:3241–3257. https://doi.org/10.1091/mbc.9.11.3241

Chen, Y., Y. Wang, J. Zhang, Y. Deng, L. Jiang, E. Song, X.S. Wu, J.A. Hammer, T. Xu, and J. Lippincott-Schwartz. 2012. Rab10 and myosin-Va mediate insulin-stimulated GLUT4 storage vesicle translocation in adipocytes. *J. Cell Biol.* 198:545–560. https://doi.org/10.1083/jcb.201111091

Deng, C.Y., W.L. Lei, X.H. Xu, X.C. Ju, Y. Liu, and Z.G. Luo. 2014. JIP1 mediates anterograde transport of Rab10 cargos during neuronal polarization. *J. Neurosci.* 34:1710–1723. https://doi.org/10.1523/JNEUROSCI.4496-13.2014

Diaz-Rohrer, B., I. Castello-Serrano, S.H. Chan, H.Y. Wang, C.R. Shurer, K.R. Levental, and I. Levental. 2023. Rab3 mediates a pathway for endocytic sorting and plasma membrane recycling of ordered microdomains. *Proc. Natl. Acad. Sci. USA.* 120:e2207461120. https://doi.org/10.1073/pnas.2207461120

Dickinson, D.J., A.M. Pani, J.K. Heppert, C.D. Higgins, and B. Goldstein. 2015. Streamlined genome engineering with a self-excising drug selection cassette. *Genetics.* 200:1035–1049. https://doi.org/10.1534/genetics.115.178335

Edidin, M. 1992. Patches, posts and fences: Proteins and plasma membrane domains. *Trends Cell Biol.* 2:376–380. https://doi.org/10.1016/0962-8924(92)90050-W

Farmer, T., S. Xie, N. Naslavsky, J. Stöckli, D.E. James, and S. Caplan. 2021. Defining the protein and lipid constituents of tubular recycling endosomes. *J. Biol. Chem.* 296:100190. https://doi.org/10.1074/jbc.RA120.015992

Fernandes, H., E. Franklin, R. Recacha, A. Houdusse, B. Goud, and A.R. Khan. 2009. Structural aspects of Rab6-effector complexes. *Biochem. Soc. Trans.* 37:1037–1041. https://doi.org/10.1042/BST0371037

Gallegos, M.E., S. Balakrishnan, P. Chandramouli, S. Arora, A. Azameera, A. Babushekar, E. Bargoma, A. Bokhari, S.K. Chava, P. Das, et al. 2012. The C. elegans rab family: Identification, classification and toolkit construction. *PLoS One*. 7:e49387. https://doi.org/10.1371/journal.pone.0049387

Gao, J., L. Zhao, Q. Luo, S. Liu, Z. Lin, P. Wang, X. Fu, J. Chen, H. Zhang, L. Lin, and A. Shi. 2020. An EHBP-1-SID-3-DYN-1 axis promotes membranous tubule fission during endocytic recycling. *PLoS Genet.* 16:e1008763. https://doi.org/10.1371/journal.pgen.1008763

Gimona, M., K. Djinovic-Carugo, W.J. Kranewitter, and S.J. Winder. 2002. Functional plasticity of CH domains. *FEBS Lett.* 513:98–106. https://doi.org/10.1016/S0014-5793(01)03240-9

Gong, T., Y. Yan, J. Zhang, S. Liu, H. Liu, J. Gao, X. Zhou, J. Chen, and A. Shi. 2018. PTRN-1/CAMSAP promotes CYK-1/formin-dependent actin polymerization during endocytic recycling. *EMBO J.* 37:e98556. https://doi.org/10.15252/embj.201798556

Goszczynski, B., V.V. Captan, A.M. Danielson, B.R. Lancaster, and J.D. McGhee. 2016. A 44 bp intestine-specific hermaphrodite-specific enhancer from the C. elegans vit-2 vitellogenin gene is directly regulated by ELT-2, MAB-3, FKH-9 and DAF-16 and indirectly regulated by the germline, by daf-2/insulin signaling and by the TGF-β/Sma/Mab pathway. *Dev. Biol.* 413:112–127. https://doi.org/10.1016/j.ydbio.2016.02.031

Grant, B., Y. Zhang, M.C. Paupard, S.X. Lin, D.H. Hall, and D. Hirsh. 2001. Evidence that RME-1, a conserved C. elegans EH-domain protein, functions in endocytic recycling. *Nat. Cell Biol.* 3:573–579. https://doi.org/10.1038/35078549

Grant, B.D., and J.G. Donaldson. 2009. Pathways and mechanisms of endocytic recycling. *Nat. Rev. Mol. Cell Biol.* 10:597–608. https://doi.org/10.1038/nrm2755

Grigoriev, I., K.L. Yu, E. Martinez-Sanchez, A. Serra-Marques, I. Smal, E. Meijering, J. Demmers, J. Peränen, R.J. Pasterkamp, P. van der Sluijs, et al. 2011. Rab6, Rab8, and MICAL3 cooperate in controlling docking and fusion of exocytotic carriers. *Curr. Biol.* 21:967–974. https://doi.org/10.1016/j.cub.2011.04.030

Guo, W., D. Roth, C. Walch-Solimena, and P. Novick. 1999. The exocyst is an effector for Sec4p, targeting secretory vesicles to sites of exocytosis. *EMBO J.* 18:1071–1080. https://doi.org/10.1093/emboj/18.4.1071

Hall, D.H., V.P. Winfrey, G. Blaeuer, L.H. Hoffman, T. Furuta, K.L. Rose, O. Hobert, and D. Greenstein. 1999. Ultrastructural features of the adult hermaphrodite gonad of Caenorhabditis elegans: Relations between the germ line and soma. *Dev. Biol.* 212:101–123. https://doi.org/10.1006/dbio.1999.9356

Huber, L.A., S. Pimplikar, R.G. Parton, H. Virta, M. Zerial, and K. Simons. 1993. Rab8, a small GTPase involved in vesicular traffic between the TGN and the basolateral plasma membrane. *J. Cell Biol.* 123:35–45. https://doi.org/10.1083/jcb.123.1.35

Hutagalung, A.H., and P.J. Novick. 2011. Role of Rab GTPases in membrane traffic and cell physiology. *Physiol. Rev.* 91:119–149. https://doi.org/10.1152/physrev.00059.2009

Janoueix-Lerosey, I., F. Jollivet, J. Camonis, P.N. Marche, and B. Goud. 1995. Two-hybrid system screen with the small GTP-binding protein Rab6. Identification of a novel mouse GDP dissociation inhibitor isoform and two other potential partners of Rab6. *J. Biol. Chem.* 270:14801–14808. https://doi.org/10.1074/jbc.270.24.14801

Kamath, R.S., and J. Ahringer. 2003. Genome-wide RNAi screening in Caenorhabditis elegans. *Methods*. 30:313–321. https://doi.org/10.1016/S1046-2023(03)00050-1

Kanie, T., and P.K. Jackson. 2018. Guanine nucleotide exchange assay using fluorescent MANT-GDP. *Bio Protoc.* 8:e2795. https://doi.org/10.21769/BioProtoc.2795

Kimble, J., and W.J. Sharrock. 1983. Tissue-specific synthesis of yolk proteins in Caenorhabditis elegans. *Dev. Biol.* 96:189–196. https://doi.org/10.1016/0012-1606(83)90322-6

Li, T.Y., A.W. Gao, X. Li, H. Li, Y.J. Liu, A. Lalou, N. Neelagandan, F. Naef, K. Schoonjans, and J. Auwerx. 2023. V-ATPase/TORC1-mediated ATFS-1 translation directs mitochondrial UPR activation in C. elegans. *J. Cell Biol.* 222:e202205045. https://doi.org/10.1083/jcb.202205045

Li, W., P. Yi, and G. Ou. 2015. Somatic CRISPR-Cas9-induced mutations reveal roles of embryonically essential dynein chains in Caenorhabditis elegans cilia. *J. Cell Biol.* 208:683–692. https://doi.org/10.1083/jcb.201411041

Li, X., B. Liu, Y. Wen, J. Wang, Y.R. Guo, A. Shi, and L. Lin. 2024. Coordination of RAB-8 and RAB-11 during unconventional protein secretion. *J. Cell Biol.* 223:223. https://doi.org/10.1083/jcb.202306107

Lin, S.X., B. Grant, D. Hirsh, and F.R. Maxfield. 2001. Rme-1 regulates the distribution and function of the endocytic recycling compartment in mammalian cells. *Nat. Cell Biol.* 3:567–572. https://doi.org/10.1038/35078543

Liu, H., S. Wang, W. Hang, J. Gao, W. Zhang, Z. Cheng, C. Yang, J. He, J. Zhou, J. Chen, and A. Shi. 2018. LET-413/Erbin acts as a RAB-5 effector to promote RAB-10 activation during endocytic recycling. *J. Cell Biol.* 217:299–314. https://doi.org/10.1083/jcb.201705136

Liu, O., and B.D. Grant. 2015. Basolateral endocytic recycling requires RAB-10 and AMPH-1 mediated recruitment of RAB-5 GAP TBC-2 to endosomes. *PLoS Genet.* 11:e1005514. https://doi.org/10.1371/journal.pgen.1005514

Liu, Y., X.H. Xu, Q. Chen, T. Wang, C.Y. Deng, B.L. Song, J.L. Du, and Z.G. Luo. 2013. Myosin Vb controls biogenesis of post-Golgi Rab10 carriers during axon development. *Nat. Commun.* 4:2005. https://doi.org/10.1038/ncomms3005

Lock, J.G., and J.L. Stow. 2005. Rab11 in recycling endosomes regulates the sorting and basolateral transport of E-cadherin. *Mol. Biol. Cell.* 16:1744–1755. https://doi.org/10.1091/mbc.e04-10-0867

Los, F.C., C.Y. Kao, J. Smitham, K.L. McDonald, C. Ha, C.A. Peixoto, and R.V. Aroian. 2011. RAB-5- and RAB-11-dependent vesicle-trafficking pathways are required for plasma membrane repair after attack by bacterial pore-forming toxin. *Cell Host Microbe*. 9:147–157. https://doi.org/10.1016/j.chom.2011.01.005

Lürick, A., D. Kümmel, and C. Ungermann. 2018. Multisubunit tethers in membrane fusion. *Curr. Biol.* 28:R417–R420. https://doi.org/10.1016/j.cub.2017.12.012

Manderson, A.P., J.G. Kay, L.A. Hammond, D.L. Brown, and J.L. Stow. 2007. Subcompartments of the macrophage recycling endosome direct the differential secretion of IL-6 and TNFalpha. *J. Cell Biol.* 178:57–69. https://doi.org/10.1083/jcb.200612131

Mei, K., and W. Guo. 2018. The exocyst complex. *Curr. Biol.* 28:R922–R925. https://doi.org/10.1016/j.cub.2018.06.042

Mima, J. 2021. Self-assemblies of Rab- and Arf-family small GTPases on lipid bilayers in membrane tethering. *Biophys. Rev.* 13:531–539. https://doi.org/10.1007/s12551-021-00819-4

Miserey-Lenkei, S., F. Waharte, A. Boulet, M.H. Cuif, D. Tenza, A. El Marjou, G. Raposo, J. Salamero, L. Héliot, B. Goud, and S. Monier. 2007. Rab6-interacting protein 1 links Rab6 and Rab11 function. *Traffic*. 8:1385–1403. https://doi.org/10.1111/j.1600-0854.2007.00612.x

Moyer, B.D., B.B. Allan, and W.E. Balch. 2001. Rab1 interaction with a GM130 effector complex regulates COPII vesicle cis--Golgi tethering. *Traffic*. 2:268–276. https://doi.org/10.1034/j.1600-0854.2001.1o007.x

Murray, D.H., M. Jahnel, J. Lauer, M.J. Avellaneda, N. Brouilly, A. Cezanne, H. Morales-Navarrete, E.D. Perini, C. Ferguson, A.N. Lupas, et al. 2016. An endosomal tether undergoes an entropic collapse to bring vesicles together. *Nature*. 537:107–111. https://doi.org/10.1038/nature19326

Murray, R.Z., J.G. Kay, D.G. Sangermani, and J.L. Stow. 2005. A role for the phagosome in cytokine secretion. *Science*. 310:1492–1495. https://doi.org/10.1126/science.1120225

Nickerson, D.P., C.L. Brett, and A.J. Merz. 2009. Vps-C complexes: Gatekeepers of endolysosomal traffic. *Curr. Opin. Cell Biol.* 21:543–551. https://doi.org/10.1016/j.ceb.2009.05.007

Nokes, R.L., I.C. Fields, R.N. Collins, and H. Fölsch. 2008. Rab13 regulates membrane trafficking between TGN and recycling endosomes in polarized epithelial cells. *J. Cell Biol.* 182:845–853. https://doi.org/10.1083/jcb.200802176

Pant, S., M. Sharma, K. Patel, S. Caplan, C.M. Carr, and B.D. Grant. 2009. AMPH-1/Amphiphysin/Bin1 functions with RME-1/Ehd1 in endocytic recycling. *Nat. Cell Biol.* 11:1399–1410. https://doi.org/10.1038/ncb1986

Pereira, C., D. Stalder, G.S.F. Anderson, A.S. Shun-Shion, J. Houghton, R. Antrobus, M.A. Chapman, D.J. Fazakerley, and D.C. Gershlick. 2023. The exocyst complex is an essential component of the mammalian constitutive secretory pathway. *J. Cell Biol.* 222:e202205137. https://doi.org/10.1083/jcb.202205137

Perez, M.F., M. Francesconi, C. Hidalgo-Carcedo, and B. Lehner. 2017. Maternal age generates phenotypic variation in Caenorhabditis elegans. *Nature*. 552:106–109. https://doi.org/10.1038/nature25012

Podinovskaia, M., C. Prescianotto-Baschong, D.P. Buser, and A. Spang. 2021. A novel live-cell imaging assay reveals regulation of endosome maturation. *Elife*. 10:e70982. https://doi.org/10.7554/eLife.70982

Rai, A., N. Bleimling, I.R. Vetter, and R.S. Goody. 2020. The mechanism of activation of the actin binding protein EHBP1 by Rab8 family members. *Nat. Commun.* 11:4187. https://doi.org/10.1038/s41467-020-17792-3

Rual, J.F., J. Ceron, J. Koreth, T. Hao, A.S. Nicot, T. Hirozane-Kishikawa, J. Vandenhaute, S.H. Orkin, D.E. Hill, S. van den Heuvel, and M. Vidal. 2004. Toward improving Caenorhabditis elegans phenome mapping with an ORFeome-based RNAi library. *Genome Res.* 14:2162–2168. https://doi.org/10.1101/gr.2505604

Sano, H., G.R. Peck, A.N. Kettenbach, S.A. Gerber, and G.E. Lienhard. 2011. Insulin-stimulated GLUT4 protein translocation in adipocytes requires the Rab10 guanine nucleotide exchange factor Dennd4C. *J. Biol. Chem.* 286:16541–16545. https://doi.org/10.1074/jbc.C111.228908

Sato, T., T. Iwano, M. Kunii, S. Matsuda, R. Mizuguchi, Y. Jung, H. Hagiwara, Y. Yoshihara, M. Yuzaki, R. Harada, and A. Harada. 2014. Rab8a and Rab8b are essential for several apical transport pathways but insufficient for ciliogenesis. *J. Cell Sci.* 127:422–431. https://doi.org/10.1242/jcs.136903

Satoh, A.K., J.E. O'Tousa, K. Ozaki, and D.F. Ready. 2005. Rab11 mediates post-Golgi trafficking of rhodopsin to the photosensitive apical membrane of Drosophila photoreceptors. *Development*. 132:1487–1497. https://doi.org/10.1242/dev.01704

Schuck, S., M.J. Gerl, A. Ang, A. Manninen, P. Keller, I. Mellman, and K. Simons. 2007. Rab10 is involved in basolateral transport in polarized Madin-Darby canine kidney cells. *Traffic*. 8:47–60. https://doi.org/10.1111/j.1600-0854.2006.00506.x

Shi, A., C.C. Chen, R. Banerjee, D. Glodowski, A. Audhya, C. Rongo, and B.D. Grant. 2010. EHBP-1 functions with RAB-10 during endocytic recycling in Caenorhabditis elegans. *Mol. Biol. Cell*. 21:2930–2943. https://doi.org/10.1091/mbc.e10-02-0149

Shi, A., O. Liu, S. Koenig, R. Banerjee, C.C. Chen, S. Eimer, and B.D. Grant. 2012. RAB-10-GTPase-mediated regulation of endosomal phosphatidylinositol-4,5-bisphosphate. *Proc. Natl. Acad. Sci. USA*. 109:E2306–E2315. https://doi.org/10.1073/pnas.1205278109

Shvarev, D., J. Schoppe, C. König, A. Perz, N. Füllbrunn, S. Kiontke, L. Langemeyer, D. Januliene, K. Schnelle, D. Kümmel, et al. 2022. Structure of the HOPS tethering complex, a lysosomal membrane fusion machinery. *Elife*. 11:e80901. https://doi.org/10.7554/eLife.80901

Simonsen, A., R. Lippé, S. Christoforidis, J.M. Gaullier, A. Brech, J. Callaghan, B.H. Toh, C. Murphy, M. Zerial, and H. Stenmark. 1998. EEA1 links PI(3)K function to Rab5 regulation of endosome fusion. *Nature*. 394:494–498. https://doi.org/10.1038/28879

Solinger, J.A., H.O. Rashid, C. Prescianotto-Baschong, and A. Spang. 2020. FERARI is required for Rab11-dependent endocytic recycling. *Nat. Cell Biol.* 22:213–224. https://doi.org/10.1038/s41556-019-0456-5

Solinger, J.A., H.O. Rashid, and A. Spang. 2022. FERARI and cargo adaptors coordinate cargo flow through sorting endosomes. *Nat. Commun.* 13:4620. https://doi.org/10.1038/s41467-022-32377-y

Spang, A. 2002. ARF1 regulatory factors and COPI vesicle formation. *Curr. Opin. Cell Biol.* 14:423–427. https://doi.org/10.1016/S0955-0674(02)00346-0

Spang, A. 2008. The life cycle of a transport vesicle. *Cell. Mol. Life Sci.* 65:2781–2789. https://doi.org/10.1007/s00018-008-8349-y

Spang, A. 2012. The DSL1 complex: The smallest but not the least CATCHR. *Traffic*. 13:908–913. https://doi.org/10.1111/j.1600-0854.2012.01362.x

Spang, A. 2016. Membrane tethering complexes in the endosomal system. *Front. Cell Dev. Biol.* 4:35. https://doi.org/10.3389/fcell.2016.00035

Sun, L., O. Liu, J. Desai, F. Karbassi, M.A. Sylvain, A. Shi, Z. Zhou, C.E. Rocheleau, and B.D. Grant. 2012. CED-10/Rac1 regulates endocytic recycling through the RAB-5 GAP TBC-2. *PLoS Genet.* 8:e1002785. https://doi.org/10.1371/journal.pgen.1002785

Szentgyörgyi, V., and A. Spang. 2023. Membrane tethers at a glance. *J. Cell Sci.* 136:jcs260471. https://doi.org/10.1242/jcs.260471

Szumowski, S.C., M.R. Botts, J.J. Popovich, M.G. Smelkinson, and E.R. Troemel. 2014. The small GTPase RAB-11 directs polarized exocytosis of the intracellular pathogen N. parisii for fecal-oral transmission from C. elegans. *Proc. Natl. Acad. Sci. USA*. 111:8215–8220. https://doi.org/10.1073/pnas.1400696111

Takacs, C.N., U. Andreo, V.L. Dao Thi, X. Wu, C.E. Gleason, M.S. Itano, G.S. Spitz-Becker, R.L. Belote, B.R. Hedin, M.A. Scull, et al. 2017. Differential regulation of lipoprotein and hepatitis C Virus secretion by Rab1b. *Cell Rep.* 21:431–441. https://doi.org/10.1016/j.celrep.2017.09.053

Takenaka, M., H. Inoue, A. Takeshima, T. Kakura, and T. Hori. 2013. C. elegans Rassf homolog, rasf-1, is functionally associated with rab-39 Rab GTPase in oxidative stress response. *Genes Cells*. 18:203–210. https://doi.org/10.1111/gtc.12028

Tao, T., J. Sun, Y. Peng, Y. Li, P. Wang, X. Chen, W. Zhao, Y.Y. Zheng, L. Wei, W. Wang, et al. 2019. Golgi-resident TRIO regulates membrane trafficking during neurite outgrowth. *J. Biol. Chem.* 294:10954–10968. https://doi.org/10.1074/jbc.RA118.007318

Taylor, C.A., J. Yan, A.S. Howell, X. Dong, and K. Shen. 2015. RAB-10 regulates dendritic branching by balancing dendritic transport. *PLoS Genet.* 11:e1005695. https://doi.org/10.1371/journal.pgen.1005695

Thompson, A., R. Nessler, D. Wisco, E. Anderson, B. Winckler, and D. Sheff. 2007. Recycling endosomes of polarized epithelial cells actively sort apical and basolateral cargos into separate subdomains. *Mol. Biol. Cell*. 18:2687–2697. https://doi.org/10.1091/mbc.e05-09-0873

Upadhyay, A.K., P.P. Borbat, J. Wang, J.H. Freed, and D.E. Edmondson. 2008. Determination of the oligomeric states of human and rat monoamine oxidases in the outer mitochondrial membrane and octyl beta-D-glucopyranoside micelles using pulsed dipolar electron spin resonance spectroscopy. *Biochemistry*. 47:1554–1566. https://doi.org/10.1021/bi7021377

Wang, P., H. Liu, Y. Wang, O. Liu, J. Zhang, A. Gleason, Z. Yang, H. Wang, A. Shi, and B.D. Grant. 2016. RAB-10 promotes EHBP-1 bridging of filamentous actin and tubular recycling endosomes. *PLoS Genet.* 12:e1006093. https://doi.org/10.1371/journal.pgen.1006093

Wang, S., L. Yao, W. Zhang, Z. Cheng, C. Hu, H. Liu, Y. Yan, and A. Shi. 2021. AP-1 recruits SMAP-1/SMAPs to the trans-Golgi network to promote sorting in polarized epithelia. *Front. Cell Dev. Biol.* 9:774401. https://doi.org/10.3389/fcell.2021.774401

Wang, X., X. Li, J. Wang, J. Wang, C. Hu, J. Zeng, A. Shi, and L. Lin. 2022. SMGL-1/NBAS acts as a RAB-8 GEF to regulate unconventional protein secretion. *J. Cell Biol.* 221:e202111125. https://doi.org/10.1083/jcb.202111125

Watterson, A., L. Tatge, N. Wajahat, S.L.B. Arneaud, R. Solano Fonseca, S.T. Beheshti, P. Metang, M. Mihelakis, K.R. Zuurbier, C.D. Corley, et al. 2022. Intracellular lipid surveillance by small G protein geranylgeranylation. *Nature*. 605:736–740. https://doi.org/10.1038/s41586-022-04729-7

Way, M., B. Pope, and A.G. Weeds. 1992. Evidence for functional homology in the F-actin binding domains of gelsolin and alpha-actinin: Implications for the requirements of severing and capping. *J. Cell Biol.* 119:835–842. https://doi.org/10.1083/jcb.119.4.835

Wells, A., C.C. Mendes, F. Castellanos, P. Mountain, T. Wright, S.M. Wainwright, M.I. Stefana, A.L. Harris, D.C.I. Goberdhan, and C. Wilson. 2023. A Rab6 to Rab11 transition is required for dense-core granule and exosome biogenesis in Drosophila secondary cells. *PLoS Genet.* 19:e1010979. https://doi.org/10.1371/journal.pgen.1010979

Winder, S.J., L. Hemmings, S.K. Maciver, S.J. Bolton, J.M. Tinsley, K.E. Davies, D.R. Critchley, and J. Kendrick-Jones. 1995. Utrophin actin binding domain: Analysis of actin binding and cellular targeting. *J. Cell Sci.* 108:63–71. https://doi.org/10.1242/jcs.108.1.63

Wong, M., and S. Munro. 2014. Membrane trafficking. The specificity of vesicle traffic to the Golgi is encoded in the golgin coiled-coil proteins. *Science*. 346:1256898. https://doi.org/10.1126/science.1256898

Xu, S., Z. Wang, K.W. Kim, Y. Jin, and A.D. Chisholm. 2016. Targeted mutagenesis of duplicated genes in Caenorhabditis elegans using CRISPR-Cas9. *J. Genet. Genomics*. 43:103–106. https://doi.org/10.1016/j.jgg.2015.11.004

Yan, Y., S. Liu, C. Hu, C. Xie, L. Zhao, S. Wang, W. Zhang, Z. Cheng, J. Gao, X. Fu, et al. 2021. RTKN-1/Rhotekin shields endosome-associated F-actin from disassembly to ensure endocytic recycling. *J. Cell Biol.* 220:e202007149. https://doi.org/10.1083/jcb.202007149

Yoshimura, S., A. Gerondopoulos, A. Linford, D.J. Rigden, and F.A. Barr. 2010. Family-wide characterization of the DENN domain Rab GDP-GTP exchange factors. *J. Cell Biol.* 191:367–381. https://doi.org/10.1083/jcb.201008051

Yu, I.M., and F.M. Hughson. 2010. Tethering factors as organizers of intracellular vesicular traffic. *Annu. Rev. Cell Dev. Biol.* 26:137–156. https://doi.org/10.1146/annurev.cellbio.042308.113327

Zhang, J., Z. Jiang, C. Chen, L. Yao, Z. Gao, Z. Cheng, Y. Yan, H. Liu, and A. Shi. 2023. Age-associated decline in RAB-10 efficacy impairs intestinal barrier integrity. *Nat. Aging*. 3:1107–1127. https://doi.org/10.1038/s43587-023-00475-1

Zhang, W., S. Wang, C. Yang, C. Hu, D. Chen, Q. Luo, Z. He, Y. Liao, Y. Yao, J. Chen, et al. 2020. LET-502/ROCK regulates endocytic recycling by promoting activation of RAB-5 in a distinct subpopulation of sorting endosomes. *Cell Rep.* 32:108173. https://doi.org/10.1016/j.celrep.2020.108173

Zou, W., S. Yadav, L. DeVault, Y. Nung Jan, and D.R. Sherwood. 2015. RAB-10-Dependent membrane transport is required for dendrite arborization. *PLoS Genet.* 11:e1005484. https://doi.org/10.1371/journal.pgen.1005484

Supplemental material

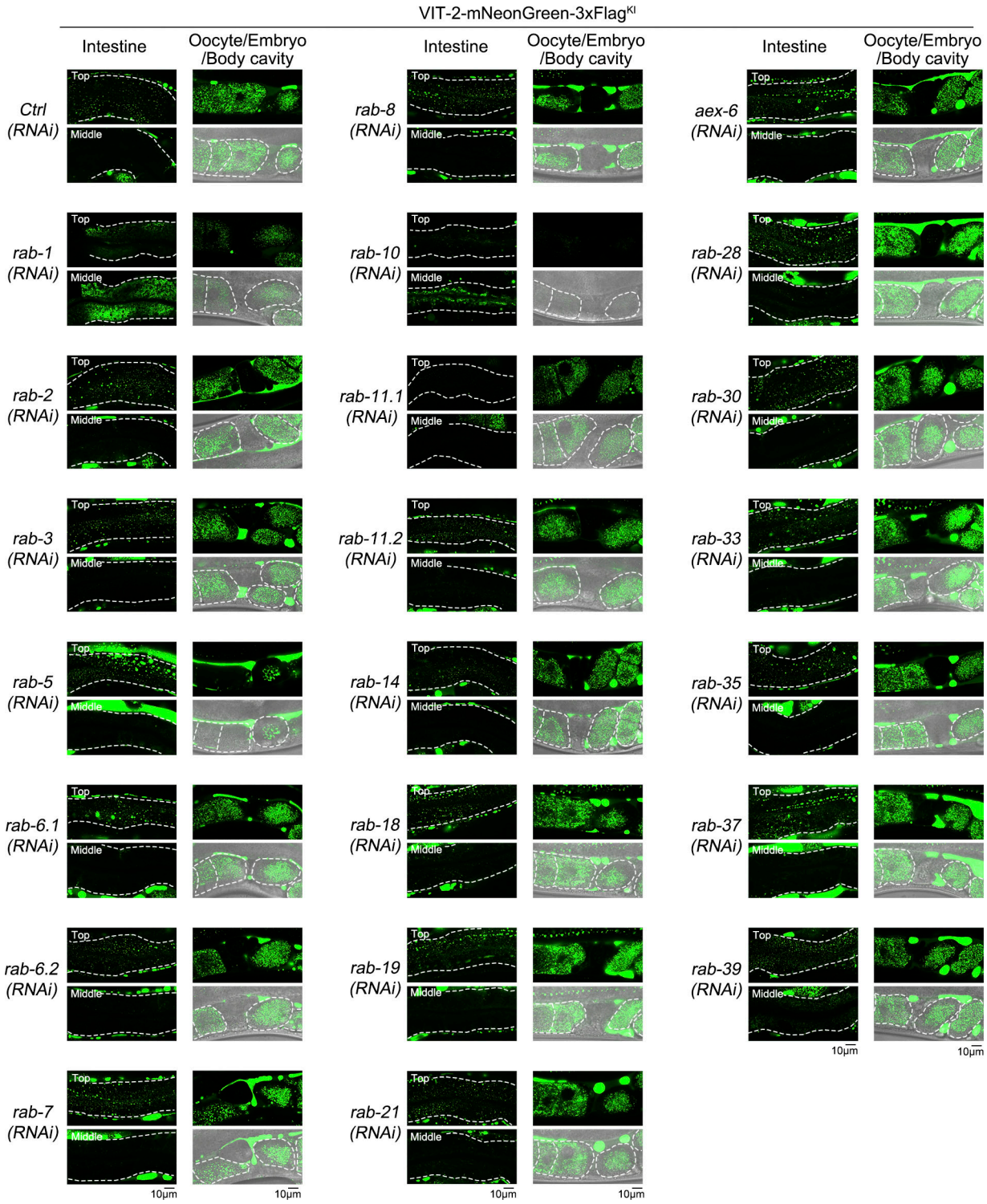

Figure S1. **Yolk exocytosis-regulating RNAi screening on 22 Rabs.** Confocal images showing the distribution of VIT-2-mNeonGreen-3xFlag^{KI} in the *C. elegans* intestine, oocytes, and embryos in various Rab knockdown backgrounds. White dashed lines indicate the outlines of the intestine, oocytes, or embryos.

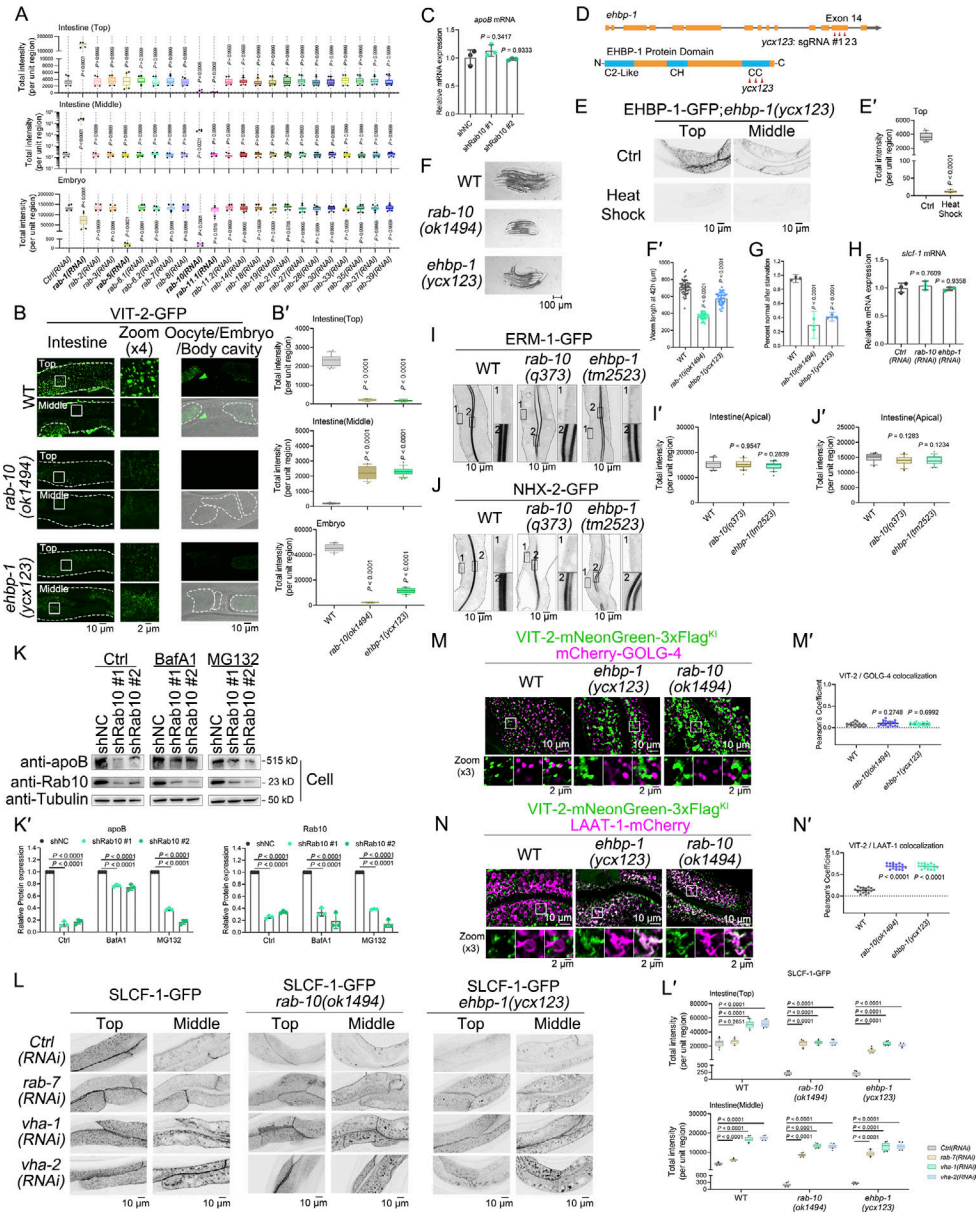

Figure S2. **RAB-10 and EHBP-1 are not involved in apical exocytosis. (A)** Statistical analysis data of Fig. S1 is shown as box-and-whisker plots with 10th–90th percentile (n = 24 cells from eight animals of each genotype; dots, outliers; boundaries, quartiles; one-way ANOVA test with Dunn's multiple comparison). **(B and B′)** Confocal images showing the distribution of VIT-2-GFP in the *C. elegans* intestine, oocytes, and embryos in different gene knockdown backgrounds. Statistical data is shown as box-and-whisker plots with 10th–90th percentile (n = 24 cells from eight animals of each genotype; dots, outliers; boundaries, quartiles; one-way ANOVA test with Dunn's multiple comparison). **(C)** mRNA level of apoB in different genetic backgrounds in HepG2 cells. Error bars represent 95% CIs (one-way ANOVA test with Dunn's multiple comparison). **(D)** Genomic structure of *C. elegans ehbp-1* and CRISPR-Cas9 targeting site of *ycx123*. **(E and E′)** Confocal images showing EHBP-1-GFP-labeled structures. The statistical data are shown as box-and-whisker plots with the 10th–90th percentile (n = 24 cells from eight animals of each genotype; dots, outliers; boundaries, quartiles; two-tailed Mann-Whitney test). **(F and F′)** The growth speed of offspring from 1-day-old mothers was measured by their body length at 42 h after hatching. The error bars represent 95% CIs (n = 50 animals; one-way ANOVA test with Dunn's multiple comparison). **(G)** The percentage of animals achieving normal development after starvation of L1 larvae. Data were acquired from three independent experiments using 300 animals for each genetic background. Error bars represent 95% CIs (n = 50 animals; one-way ANOVA test with Dunn's multiple comparison). **(H)** mRNA level of *slcf-1* in different gene knockdown backgrounds in *C. elegans*. Error bars represent 95% CIs (one-way ANOVA test with Dunn's multiple comparison). **(I and I′)** Confocal images showing the subcellular localization of ERM-1-GFP. **(J and J′)** Confocal images showing the subcellular localization of NHX-2-GFP. Statistical data are shown as box-and-whisker plots with 10th–90th percentile (n = 24 cells from eight animals of each genotype; dots, outliers; boundaries, quartiles; one-way ANOVA test with Dunn's multiple comparison). **(K and K′)** Western blot analysis of apoB protein levels in Huh7 cells. Band intensity was measured using the "Plot Lanes" function in ImageJ from three independent experiments. Error bars represent 95% CIs (one-way ANOVA test with Dunn's multiple comparison). **(L and L′)** Confocal images showing the subcellular localization of SLCF-1-GFP. Statistical data is shown as box-and-whisker plots with 10th–90th percentile (n = 24 cells from eight animals of each genotype; dots, outliers; boundaries, quartiles; two-way ANOVA with Bonferroni post-test). **(M–N′)** Confocal images showing the colocalization between VIT-2-mNeonGreen-3xFlag^{KI} and LAAT-1-mCherry or mCherry-GOLG-4. The statistical analysis of colocalization was calculated as the Pearson's correlation coefficient and is shown as the mean ± SD (n = 18 cells from six animals of each genotype; one-way ANOVA test with Dunn's multiple comparison). Source data are available for this figure: SourceData FS2.

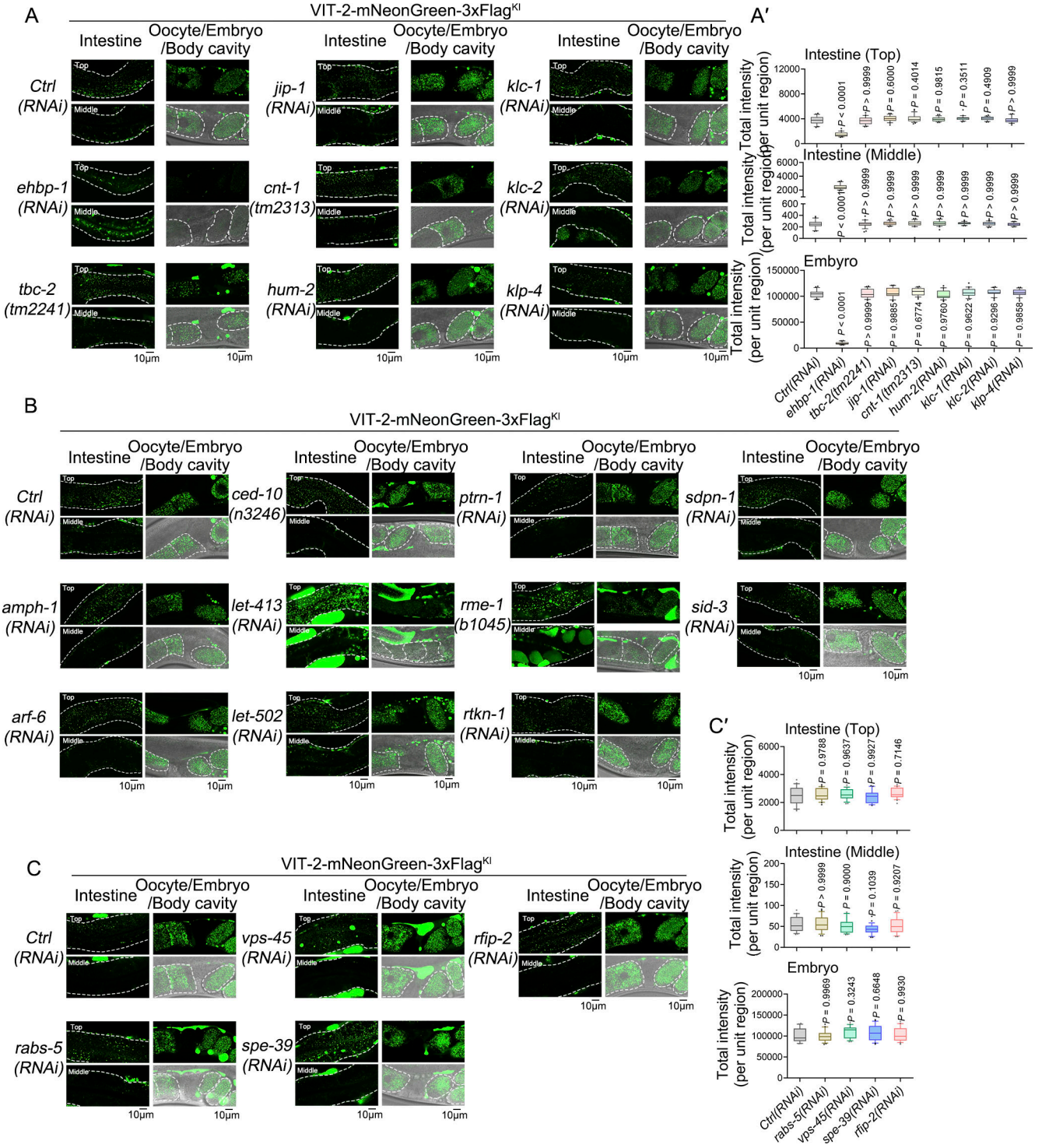

Figure S3. **Yolk exocytosis-regulating RNAi screening on recycling regulators, RAB-10 effectors and FERARIs. (A–C′)** Confocal images showing the distribution of VIT-2-mNeonGreen-3xFlag^{KI} in the *C. elegans* intestine, oocytes, and embryos in different genetic backgrounds. The statistical data are displayed as box-and-whisker plots with the 10th–90th percentile (n = 24 cells from eight animals of each genotype; dots, outliers; boundaries, quartiles; one-way ANOVA test with Dunn's multiple comparison).

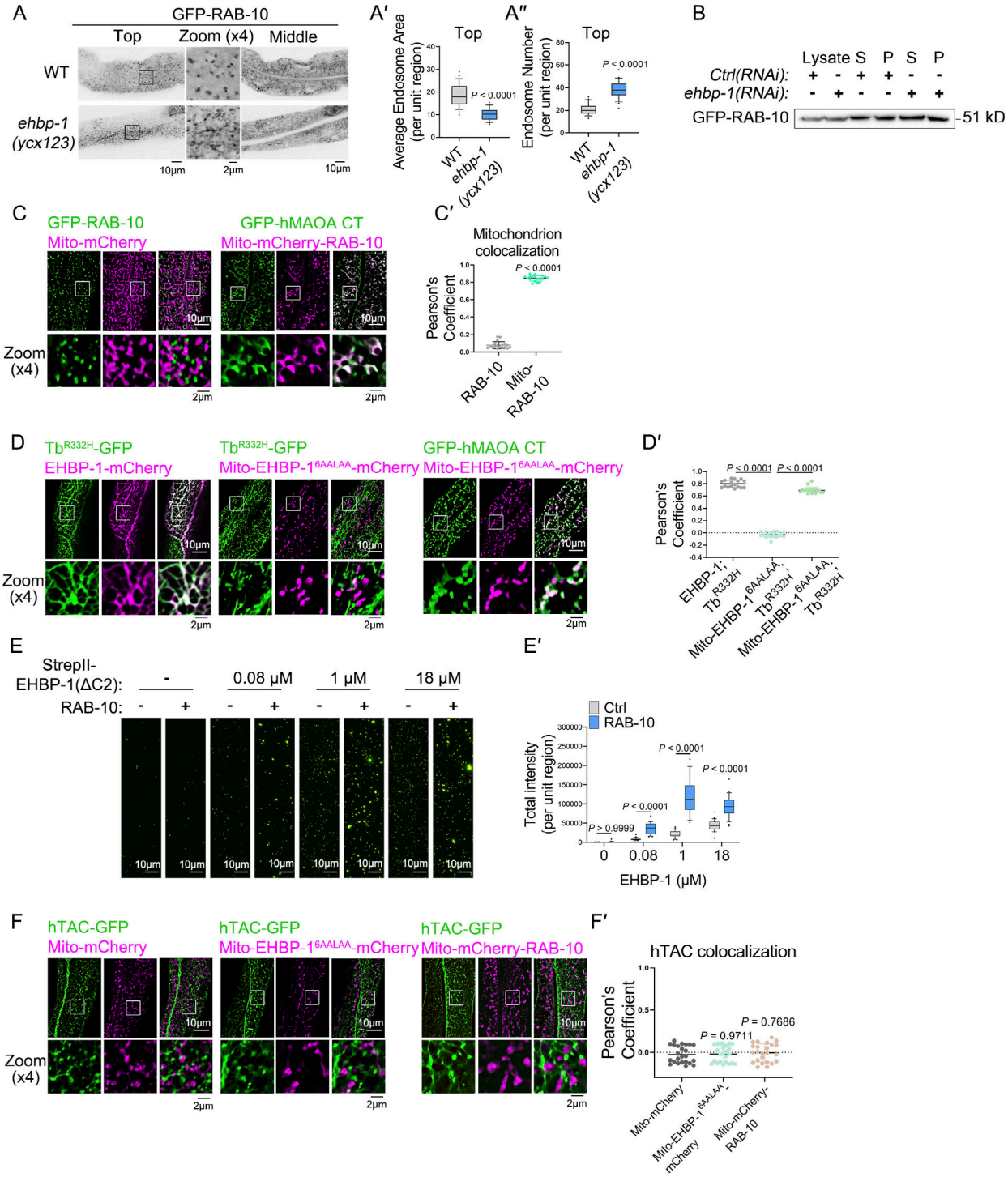

Figure S4. **EHBP-1 sequesters exocytic carriers through a mechanism dependent on RAB-10. (A–A″)** Confocal images showing the subcellular localization of GFP-RAB-10. Statistical data is shown as box-and-whisker plots with 10th–90th percentile (n = 24 cells from eight animals of each genotype; dots, outliers; boundaries, quartiles; two-tailed Mann–Whitney test). **(B)** Western blotting showing the results of membrane fractionation for GFP-RAB-10. S: supernatant; P: pellet. **(C and C′)** Confocal images showing colocalization between RAB-10 and mitochondria. The statistical analysis of colocalization was calculated as the Pearson's correlation coefficient and is shown as the mean ± SD (n = 18 cells from six animals of each genotype; two-tailed Mann-Whitney test). **(D and D′)** Confocal images showing colocalization between GFP or mCherry fusion proteins. The statistical analysis of colocalization was calculated as the Pearson's correlation coefficient and is shown as the mean ± SD (n = 18 cells from six animals of each genotype; one-way ANOVA test with Dunn's multiple comparison). **(E and E′)** The images were acquired using a TIRF microscope showing liposomes captured by slides immobilized with StrepII-EHBP-1(ΔC2). Statistical data is shown as box-and-whisker plots with the 10th–90th percentile (n = 24 areas; dots, outliers; boundaries, quartiles; two-way ANOVA with Bonferroni post-test). **(F and F′)** Confocal images showing colocalization between hTAC-GFP and Mito-mCherry or Mito-EHBP-1^{6AALAA}-mCherry or Mito-mCherry-RAB-10. The statistical analysis of colocalization was calculated as the Pearson's correlation coefficient and is shown as the mean ± SD (n = 18 cells from six animals of each genotype; one-way ANOVA test with Dunn's multiple comparison). Source data are available for this figure: SourceData FS4.

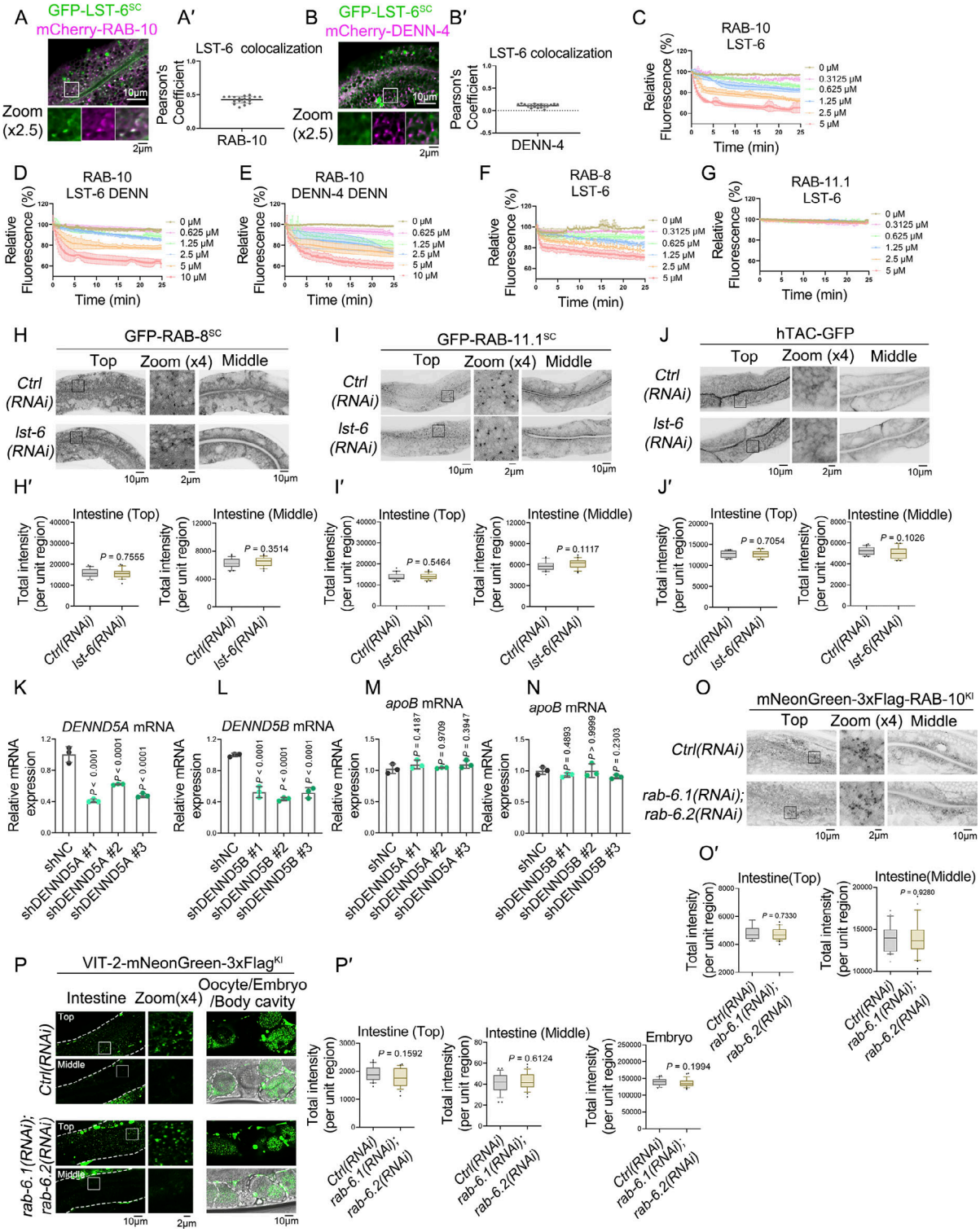

Figure S5. **LST-6/DENND5 functions as a guanine nucleotide exchange factor (GEF) for RAB-10, facilitating exocytic transport. (A–B′)** Confocal images showing colocalization between GFP-LST-6^{SC} and mCherry-RAB-10 or mCherry-DENN-4. The statistical analysis of colocalization was calculated as Pearson's correlation coefficient, Error bars represent 95% CIs (n = 18 cells from six animals of each genotype). **(C–G)** An in vitro GEF assay was used to detect the release of MANT-GDP from RAB-10, RAB-8, and RAB-11.1, which was mediated by GST-LST-6, GST-LST-6 DENN, or GST-DENN-4 DENN. **(H–J′)** Confocal images showing the subcellular localization of GFP-RAB-8^{SC}, GFP-RAB-11.1^{SC}, and hTAC-GFP in different genetic backgrounds. Statistical data is shown as box-and-whisker plots with 10th–90th percentile (n = 24 cells from eight animals of each genotype; dots, outliers; boundaries, quartiles; two-tailed Mann–Whitney test). **(K–N)** mRNA level of DENND5A, DENND5B, apoB in different genetic backgrounds in Huh7 cells. Error bars represent 95% CIs (one-way ANOVA test with Dunn's multiple comparison). **(O–P′)** Confocal images showing the subcellular localization of mNeonGreen-3xFlag-RAB-10^{KI} or VIT-2-mNeonGreen-3xFlag^{KI} in different genetic backgrounds. Statistical data is shown as box-and-whisker plots with 10th–90th percentile (n = 24 cells from eight animals of each genotype; dots, outliers; boundaries, quartiles; two-tailed Mann–Whitney test).

Video 1. **Imaging of GFP-RAB-10-labeled endosomes in the intestinal cell of wild-type *C. elegans*.** Spanning disk confocal was used for image acquisition with a 0.8-s interval. Images have been denoised and deconvolved using NIS Elements AR 5.30.00. Playback 7 fps. This video is associated with Fig. 3 F.

Video 2. **Imaging of GFP-RAB-10-labeled endosomes in the intestinal cell of *ycx123* mutant animal.** Spanning disk confocal was used for image acquisition with a 0.8-s interval. Images have been denoised and deconvolved using NIS Elements AR 5.30.00. Playback 7 fps. This video is associated with Fig. 3 F.

Provided online are Table S1 and Table S2. Table S1 provides a list of the *C. elegans* strains utilized in the study. Table S2 presents the qPCR primers and corresponding results.